

A unified SPH framework for shell-related interactions

Dong Wu^a, Shuaihao Zhang^b, Weiyi Kong^c, Xiangyu Hu^{a,*}

^a*Chair of Aerodynamics and Fluid Mechanics, Technical University of Munich, 85748 Garching, Germany*

^b*Department of Civil and Environmental Engineering, Hong Kong University of Science and Technology, Clearwater Bay, Kowloon, Hong Kong SAR, China*

^c*Virtonomy GmbH, 80336 Munich, Germany*

Abstract

A unified Smoothed Particle Hydrodynamics (SPH) framework is proposed to simulate interaction dynamics involving thin shells modeled by a reduced-dimensional, single-layer particle discretization, as opposed to full-dimensional SPH solids. The framework encompasses one-sided fluid–shell interactions, with the fluid present on only one side of the shell, as well as solid–shell, shell–shell, and shell-self interactions. The study introduces a novel concept of imaginary shell contact particles, generated by projecting real shell particles along the local normal direction within the cut-off radius of the fluid particle, thereby mapping this reduced-dimensional shell model into a full-dimensional representation. With the volume of the imaginary particles defined based on the local shell curvature, the projection preserves kernel completeness for fluid-shell interactions while leaving the fluid-structure interaction (FSI) dynamics unchanged, such that the fluid-shell coupling algorithm is the same as in standard fluid-solid coupling. In addition, a particle-to-particle contact

*Corresponding author.

Email addresses: dong.wu@tum.de (Dong Wu), shzhangce@ust.hk (Shuaihao Zhang), kong@virtonomy.io (Weiyi Kong), xiangyu.hu@tum.de (Xiangyu Hu)

model for solid-solid interactions is developed by analogy to fluid dynamics: a contact density is computed using a fluid-style density initialization, and the resulting contact forces follow a momentum-equation-inspired formulation. Combined with the projection strategy, this contact formulation is directly extended to efficiently handle shell-related contact problems. The proposed method is validated using a series of benchmark tests, demonstrating stable and accurate performance across diverse interaction scenarios.

Keywords: Fluid-shell interaction, Solid-shell contact, Shell-shell contact, Shell-self contact, SPH.

1. Introduction

Smoothed Particle Hydrodynamics (SPH), a fully Lagrangian and mesh-free method, has attracted increasing attention over recent decades [1, 2, 3, 4, 5]. In SPH, continua are discretized into particles, and the governing equations solved via particle interactions mediated by a Gaussian-like kernel function [6, 7, 8]. Owing to its particle-interaction-based formulation, which aligns naturally with abstractions underlying a wide range of physical systems, SPH has proven particularly effective for multi-physics simulations within a unified computational framework [9, 10].

Fluid–structure interaction (FSI), particularly involving flexible and deformable elastic structures, represents a typical multi-physical system in which fluid and structural dynamics are tightly coupled. Due to the intrinsic complexity of the surrounding flow and the potentially large deformation of the structure, computational studies of FSI problems remain highly challenging. Accordingly, much of the SPH literature has focused on

fluid–structure coupling [11, 12, 13, 14, 15, 16, 17, 18, 19]. In these models, pressure and viscous forces across the fluid–structure interface are typically evaluated [20, 13, 21], and density initialization schemes are often adapted in the presence of structure boundaries to alleviate kernel truncation effects [22, 23, 24].

In many practical FSI scenarios, structural dynamics also involve contact between interacting bodies or self-contact. Existing SPH contact methods can generally be categorized into particle-to-particle and particle-to-segment approaches [25]. In particle-to-particle contact, particles are idealized as rigid spheres and penalty forces are introduced to prevent interpenetration [26, 27, 28]. In particle-to-segment contact, normal penalty forces are defined with respect to a segment-based surface representation, which facilitates the incorporation of friction [29, 30, 31].

Despite the progress in SPH-based FSI and structural contact modeling, interactions involving shells, which are thin structures modeled by reduced-dimensional, single-layer particle discretizations, remain comparatively less explored compared with those for full-dimensional SPH solids. Owing to their thin-walled nature and reduced-dimensional representation, shells pose additional challenges for both fluid coupling and contact modeling. Only a limited number of studies have demonstrated the capability of SPH to capture deformation of shell structures under fluid loading, as well as the feedback of shell motion on the surrounding flow [26, 32, 33, 34, 35, 36]. Two strategies are most commonly adopted. One is the normal-flux method [37], which distinguishes neighboring fluid particles located on opposite sides of a shell and has mainly been used for two-sided FSI, where the shell is wetted

by fluid on both sides [33, 35, 36]. The other is a particle-to-particle contact-based treatment, which has been employed primarily for one-sided FSI and has also been used in example settings involving solid-shell contact [26, 32].

Nevertheless, a unified treatment covering fluid-shell coupling together with solid-shell, shell-shell, and shell-self contact is still lacking. In this paper, we propose a unified SPH framework for shell-related interaction dynamics. The framework introduces imaginary shell contact particles by projecting real shell particles along the local normal direction within a fluid particle's cut-off radius, thereby mapping the reduced-dimensional shell model into an effective full-dimensional representation. The volume of these imaginary particles is determined from the local shell curvature, which preserves kernel completeness for fluid particles near the shell boundary while leaving the underlying FSI dynamics unchanged, so that fluid-shell coupling follows the same algorithm as standard fluid-solid coupling. In addition, a particle-to-particle contact model for solid-solid interactions is developed by analogy to fluid dynamics, where a contact density is computed using a fluid-style density initialization and the corresponding contact forces follow a momentum-equation-inspired formulation. Combined with the projection strategy, this contact formulation is directly extended to efficiently handle shell-related contact problems. The proposed framework is validated through a series of benchmark tests, demonstrating stability, accuracy, and versatility across diverse interaction scenarios. In addition, a complex industrial case study, a half-filled oil tank impacted by a struck, is simulated to further showcase the applicability of the proposed formulation, involving both FSI and contact events.

The structure of this paper is as follows. Section 2 describes the governing equations for fluid, solid, and shell models. The interaction models including preliminary working of the fluid-solid interaction framework and the present shell-related interaction models are detailed in Section 3. Numerical examples are presented and discussed in Section 4. Section 5 concludes the paper with a summary and outlook. To support future research and reproducibility, all computational codes utilized in this study are publicly available through the SPHinXsys [9, 38] project website at <https://www.sphinxsys.org>.

2. Governing equations

Before moving to detailed description of the interaction modeling, we first introduce the governing equations for fluid, solid and shell dynamics.

2.1. Fluid dynamics equations

The governing equations in updated Lagrangian formulation for an isothermal and Newtonian fluid flow are the mass conservation equation

$$\frac{d\rho}{dt} = -\rho\nabla \cdot \mathbf{v}, \quad (1)$$

and the momentum conservation equation

$$\rho \frac{d\mathbf{v}}{dt} = -\nabla p + \eta \nabla^2 \mathbf{v}, \quad (2)$$

where ρ is the density, t the time, \mathbf{v} the velocity, p the pressure, η the dynamics viscosity, and $d(\bullet)/dt = \partial(\bullet)/\partial t + \mathbf{v} \cdot \nabla(\bullet)$ refers to the material derivative. An artificial equation of state (EoS) for weakly compressible flows is used to close the system of Eqs. (1) and (2) as

$$p = c^{F^2} (\rho - \rho_0). \quad (3)$$

Here, ρ_0 is the initial density, and c^F denotes the artificial sound speed. Setting $c^F = 10U_{max}$, where U_{max} represents the anticipated maximum fluid speed, fulfills the weakly compressible assumption where the density variation remains around 1% [39].

2.2. Solid dynamics equations

Following the convention in continuum mechanics, the initial position \mathbf{r}^0 of a material point is defined in the initial reference configuration, and the current position \mathbf{r} in the deformed current configuration. Then the displacement \mathbf{u} of a material point, which is obtained by the difference between its current position and initial reference position, can be obtained as

$$\mathbf{u} = \mathbf{r} - \mathbf{r}^0. \quad (4)$$

Thus, the deformation tensor, is defined by

$$\mathbb{F} = \nabla^0 \mathbf{u} + \mathbb{I}, \quad (5)$$

where \mathbb{I} denotes the identity matrix, and $\nabla^0 \equiv \frac{\partial}{\partial \mathbf{r}^0}$ stands for the gradient operator with respect to the initial reference configuration. In the total Lagrangian formulation, the mass conservation equation is given by

$$\rho - \rho^0 J^{-1} = 0, \quad (6)$$

where ρ^0 is the initial reference density and $J = \det(\mathbb{F})$ the Jacobian determinant of deformation tensor \mathbb{F} . The momentum conservation equation reads

$$\rho^0 \frac{d\mathbf{v}}{dt} = \nabla^0 \cdot \mathbb{P}, \quad (7)$$

where \mathbb{P} denotes the first Piola-Kirchhoff stress tensor, which relates the forces in the current configuration to the areas in the initial reference configuration. For an ideal elastic or Kirchhoff material, \mathbb{P} is given by

$$\mathbb{P} = \mathbb{F}\mathbb{S}, \quad (8)$$

where \mathbb{S} represents the second Piola-Kirchhoff stress which is evaluated via the constitutive equation relating \mathbb{F} with the Green-Lagrangian strain tensor \mathbb{E} , defined as

$$\mathbb{E} = \frac{1}{2} (\mathbb{F}^T \mathbb{F} - \mathbb{I}). \quad (9)$$

In particular, when the material is linear elastic and isotropic, the constitutive equation is simply given by

$$\begin{aligned} \mathbb{S} &= K \operatorname{tr}(\mathbb{E}) \mathbb{I} + 2G \left(\mathbb{E} - \frac{1}{3} \operatorname{tr}(\mathbb{E}) \mathbb{I} \right) \\ &= \lambda \operatorname{tr}(\mathbb{E}) \mathbb{I} + 2\mu \mathbb{E}, \end{aligned} \quad (10)$$

where λ and μ are Lemé parameters, $K = \lambda + (2\mu/3)$ the bulk modulus and $G = \mu$ the shear modulus. The relation between the two modulus is given by

$$E = 2G(1 + 2\nu) = 3K(1 - 2\nu) \quad (11)$$

with E denotes the Young's modulus and ν the Poisson ratio. Note that the sound speed of solid structure is defined as $c^S = \sqrt{\frac{K}{\rho}}$.

2.3. Shell dynamics equations

The Uflyand–Mindlin plate theory [40, 41] is considered to account for transverse shear stress which is significant for moderately thick plates and shells. The theory implies that the thin-structure behavior can be represented by one layer of material points at its mid-surface.

We introduce \mathbf{X} to represent the global coordinate system, and $\boldsymbol{\xi}$ and \mathbf{x} , associated with so-called pseudo-normal vector \mathbf{n} of shell, to denote the initial and current local coordinate systems, respectively. The kinematics of shell can be constructed in the local coordinates denoted with the superscript $(\bullet)^L$. Each material point possesses degrees of freedom: the translation \mathbf{u}^L and rotation $\boldsymbol{\theta}^L$. The pseudo-normal vector is also presented in initial local coordinates by \mathbf{n}^L . The local position \mathbf{r}^L of a material point can be expressed as

$$\mathbf{r}^L = \mathbf{r}_m^L + \chi \mathbf{n}^L, \quad \chi \in [-d^0/2, d^0/2], \quad (12)$$

where d^0 is the shell thickness, \mathbf{r}_m the position of the material point at the mid-surface with the subscript $(\bullet)_m$ denoting the mid-surface. Note that the shell thickness is assumed to be unchanged. The local displacement \mathbf{u}^L can thus be obtained by

$$\mathbf{u}^L = \mathbf{u}_m^L + \chi \Delta \mathbf{n}^L, \quad (13)$$

where $\Delta \mathbf{n}^L = \mathbf{n}^L - \mathbf{n}^{0,L}$. The local deformation gradient tensor of 3D shells can be defined as

$$\mathbb{F}^L = \mathbb{F}_m^L + \chi \mathbb{F}_n^L = \nabla^{0,L} \mathbf{r}^L + \chi (\nabla^{0,L} \mathbf{n}^L - \nabla^{0,L} \mathbf{n}^{0,L}), \quad (14)$$

where $\nabla^{0,L} \equiv \partial/\partial \boldsymbol{\xi}$ is the gradient operators defined in the initial local configuration.

With the deformation gradient tensor \mathbb{F}^L , the Eulerian Almansi strain $\boldsymbol{\epsilon}^l$ in current local coordinates can be obtained as

$$\boldsymbol{\epsilon}^l = \frac{1}{2} \mathbb{Q} (\mathbb{Q}^0)^T \left(\mathbb{I} - (\mathbb{F}^L)^{-T} (\mathbb{F}^L)^{-1} \right) \mathbb{Q}^0 \mathbb{Q}^T, \quad (15)$$

where \mathbb{Q}^0 is the orthogonal transformation matrix from the global to initial local coordinates, and \mathbb{Q} the transformation matrix from the global to current

local coordinates. Strain in the current local coordinates is required for strain and stress correction; further details are available in our previous work [42]. When the material is linear and isotropic, the Cauchy stress \mathcal{C}^l reads

$$\mathcal{C}^l = \lambda \operatorname{tr}(\mathcal{E}^l) \mathbb{I} + 2\mu \mathcal{E}^l. \quad (16)$$

The conservation equations of shell are

$$\begin{cases} d^0 \rho^0 \frac{d\mathbf{v}_m}{dt} = J_m (\mathbb{F}_m)^{-T} \nabla^0 \cdot \mathbb{N}^T \\ \frac{(d^0)^3}{12} \rho^0 \frac{d^2 \mathbf{n}}{dt^2} = J_m (\mathbb{F}_m)^{-T} \nabla^0 \cdot \mathbb{M}^T + J_m \mathbb{Q}^T \mathbf{Q}^l, \end{cases} \quad (17)$$

where $\mathbb{N} = \mathbb{Q}^T \mathbb{N}^l \mathbb{Q}$ and $\mathbb{M} = \mathbb{Q}^T \mathbb{M}^l \mathbb{Q}$ are the stress and moment resultants, respectively, in global coordinates, \mathbf{Q}^l is the shear stress resultant, and $J_m = \det(\mathbb{F}_m)$. Here, \mathbb{N}^l , \mathbb{M}^l and \mathbf{Q}^l is the integration of the Cauchy stress \mathcal{C}^l along the shell thickness, and more details are referred to our previous work [42].

3. Interaction modeling

Before moving to detailed description of the shell-related interaction method, we first briefly summarize our previous modeling of fluid-solid interaction with unified SPH formulation and more details are referred to Refs. [13, 21].

3.1. Preliminary work

3.1.1. SPH discretization

A SPH discretization of the mass and momentum conservation equations, Eqs. (1) and (2), can be respectively derived as

$$\frac{d\rho_i}{dt} = 2\rho_i \sum_j V_j (\mathbf{v}_i - \tilde{\mathbf{v}}_{ij}) \nabla_i W_{ij}^{h^F}, \quad (18)$$

and

$$m_i \frac{d\mathbf{v}_i}{dt} = -2 \sum_j V_i V_j \tilde{p}_{ij} \nabla_i W_{ij}^{h^F} + 2 \sum_j \eta V_i V_j \frac{\mathbf{v}_{ij}}{r_{ij}} \frac{\partial W_{ij}^{h^F}}{\partial r_{ij}} + \mathbf{g} + \mathbf{f}_i^{S:p}(h^F) + \mathbf{f}_i^{S:v}(h^F), \quad (19)$$

where V_i denotes the particle volume, m_i the particle mass, \mathbf{g} the body force, and $\nabla_i W_{ij}^{h^F} = \nabla_i W(\mathbf{r}_{ij}, h^F) = \frac{\partial W_{ij}^{h^F}}{\partial \mathbf{r}_{ij}} \mathbf{e}_{ij}$, where $\mathbf{r}_{ij} = \mathbf{r}_i - \mathbf{r}_j$, h^F is smoothing length of fluid, and the unit vector $\mathbf{e}_{ij} = \frac{\mathbf{r}_{ij}}{r_{ij}}$, representing the derivative of the kernel function with respect to \mathbf{r}_i , the position of particle i . Here, the inter-particle averaged velocity and pressure, $\tilde{\mathbf{v}}_{ij}$ and \tilde{p}_{ij} , can be evaluated using either a simple arithmetic average or a solution of the inter-particle Riemann problem. In this work, a low-dissipation Riemann solver is employed, and further details are provided in Ref. [43]. The terms $\mathbf{f}_i^{S:p}(h^F)$ and $\mathbf{f}_i^{S:v}(h^F)$ denote the pressure and viscous forces, respectively, exerted on fluid particle i by the solid structure.

The SPH discretization of the solid conservation Eq. (7), based on the initial configuration, can be derived as

$$m_a \frac{d\mathbf{v}}{dt} = 2 \sum_b V_a V_b \tilde{\mathbb{P}}_{ab} \nabla_a^0 W_{ab}^{h^S} + \mathbf{g} + \mathbf{f}_a^{F:p}(h^F) + \mathbf{f}_a^{F:v}(h^F), \quad (20)$$

where $\nabla_a^0 W_{ab}^{h^S} = \frac{\partial W(\mathbf{r}_{ab}^0, h^S)}{\partial \mathbf{r}_{ab}^0} \mathbf{e}_{ab}^0$ with subscripts a and b denoting solid particles and h^S the smoothing length of solid. Here, the inter-particle averaged first Piola-Kirchhoff stress $\tilde{\mathbb{P}}$ is defined as

$$\tilde{\mathbb{P}}_{ab} = \frac{1}{2} (\mathbb{P}_a \mathbb{B}_a^0 + \mathbb{P}_b \mathbb{B}_b^0), \quad (21)$$

where $\mathbb{B}_a^0 = (\sum_b (\mathbf{r}_b^0 - \mathbf{r}_a^0) \otimes \nabla_a^0 W_{ab})^{-1}$ is the correction matrix [44, 7]. Also $\mathbf{f}_a^{F:p}(h^F)$ and $\mathbf{f}_a^{F:v}(h^F)$ correspond to the fluid pressure and viscous forces acting on the solid particle a , respectively.

In fluid-structure coupling, the surrounding solid structure is behaving as a moving boundary for fluid, and the no-slip boundary condition is imposed at the fluid-structure interface. Following Refs. [20, 21], the interaction forces $\mathbf{f}_i^{S:p}(h^F)$ and $\mathbf{f}_i^{S:v}(h^F)$ acting on a fluid particle i , due to the presence of the neighboring solid particle a , can be obtained as

$$\mathbf{f}_i^{S:p}(h^F) = -2 \sum_a V_i V_a \frac{p_i \rho_a^d + p_a^d \rho_i}{\rho_i + \rho_a^d} \nabla_i W(\mathbf{r}_{ia}, h^F), \quad (22)$$

and

$$\mathbf{f}_i^{S:v}(h^F) = 2 \sum_a \eta V_i V_a \frac{\mathbf{v}_i - \mathbf{v}_a^d}{r_{ia}} \frac{\partial W(\mathbf{r}_{ia}, h^F)}{\partial r_{ia}}. \quad (23)$$

Here, the imaginary pressure p_a^d and velocity \mathbf{v}_a^d of the solid particle are defined by

$$\begin{cases} p_a^d = p_i + \rho_i \max(0, (\mathbf{g} - \frac{d\mathbf{v}_a}{dt}) \cdot \mathbf{n}^S)(\mathbf{r}_{ia} \cdot \mathbf{n}^S) \\ \mathbf{v}_a^d = 2\mathbf{v}_i - \mathbf{v}_a \end{cases}, \quad (24)$$

where \mathbf{n}^S denotes the surface normal direction of the solid structure. And the imaginary particle density ρ_a^d is calculated through the EoS presented in Eq. (3). Note that, for the calculation of fluid-structure interaction forces, we use h^F with assumption $h^F \geq h^S$. This will ensure that a fluid particle i can be searched and tagged as a neighboring particle of a solid particle a which is located in the neighborhood of particle i . Accordingly, the interaction forces $\mathbf{f}_a^{F:p}$ and $\mathbf{f}_a^{F:v}$ acting on a solid particle a are given by

$$\mathbf{f}_a^{F:p}(h^F) = -2 \sum_i V_a V_i \frac{p_a^d \rho_i + p_i \rho_a^d}{\rho_i + \rho_a^d} \nabla_a W(\mathbf{r}_{ai}, h^F), \quad (25)$$

and

$$\mathbf{f}_a^{F:v}(h^F) = 2 \sum_i \eta V_a V_i \frac{\mathbf{v}_a^d - \mathbf{v}_i}{r_{ai}} \frac{\partial W(\mathbf{r}_{ai}, h^F)}{\partial r_{ai}}. \quad (26)$$

Note that the anti-symmetric property of the derivative of the kernel function will ensure the momentum conservation for each pair of interacting particles i and a .

3.1.2. Time stepping

The dual-criteria time-stepping method [45, 24, 21] is employed to integrate the fluid equations. The fluid time step is constrained by an advection criterion Δt_{ad}^F and an acoustic criterion Δt_{ac}^F , given by

$$\Delta t_{ad}^F = 0.25 \min \left(\frac{h^F}{|\mathbf{v}|_{max}}, \frac{h^{F2}}{\eta} \right), \quad (27)$$

and

$$\Delta t_{ac}^F = 0.6 \min \left(\frac{h^F}{c^F + |\mathbf{v}|_{max}} \right). \quad (28)$$

For the solid structure, the time-step criterion is

$$\Delta t^S = 0.6 \min \left(\frac{h^S}{c^S + |\mathbf{v}|_{max}}, \sqrt{\frac{h^S}{|\frac{d\mathbf{v}}{dt}|_{max}}} \right). \quad (29)$$

In general, $\Delta t^S < \Delta t_{ac}^F$ because $c^S > c^F$. Rather than using Δt^S as a single global time step for both phases, the structural dynamics are sub-cycled within each fluid acoustic step. Specifically, during one fluid acoustic time step Δt_{ac}^F , the structure is advanced $\kappa = \left\lfloor \frac{\Delta t_{ac}^F}{\Delta t^S} \right\rfloor + 1$ times, where $\lfloor \cdot \rfloor$ denotes the integer operation.

To eliminate the mismatch in force evaluation, the imaginary pressure p_a^d and velocity \mathbf{v}_a^d in Eq. (24) are redefined as

$$\begin{cases} p_a^d = p_i + \rho_i \max(0, (\mathbf{g} - \frac{d\tilde{\mathbf{v}}_a}{dt}) \cdot \mathbf{n}^S)(\mathbf{r}_{ia} \cdot \mathbf{n}^S) \\ \mathbf{v}_a^d = 2\mathbf{v}_i - \tilde{\mathbf{v}}_a \end{cases}, \quad (30)$$

where, in Eq. (30), $\tilde{\mathbf{v}}_a$ and $\widetilde{\frac{d\mathbf{v}_a}{dt}}$ denote the time-averaged velocity and acceleration of the solid particles over one fluid acoustic time step.

A position-based Verlet scheme [45, 21] is employed. Quantities at the beginning, mid-point, and end of a fluid acoustic time step are denoted by the superscripts n , $n + \frac{1}{2}$, and $n + 1$, respectively. The fluid integration is first performed as

$$\begin{cases} \rho_i^{n+\frac{1}{2}} = \rho_i^n + \frac{1}{2}\Delta t_{ac}^F \frac{d\rho_i}{dt} \\ \mathbf{r}_i^{n+\frac{1}{2}} = \mathbf{r}_i^n + \frac{1}{2}\Delta t_{ac}^F \mathbf{v}_i^n \end{cases}, \quad (31)$$

by advancing the density and position to the mid-point. The particle velocity is then updated to the new time level as

$$\mathbf{v}_i^{n+1} = \mathbf{v}_i^n + \Delta t_{ac}^F \frac{d\mathbf{v}_i}{dt}. \quad (32)$$

Finally, the position and density of fluid particles are updated to the new time step by

$$\begin{cases} \mathbf{r}_i^{n+1} = \mathbf{r}_i^{n+\frac{1}{2}} + \frac{1}{2}\Delta t_{ac}^F \mathbf{v}_i \\ \rho_i^{n+1} = \rho_i^{n+\frac{1}{2}} + \frac{1}{2}\Delta t_{ac}^F \frac{d\rho_i}{dt} \end{cases}. \quad (33)$$

At this stage, the solid-particle acceleration induced by pressure and viscous forces is assumed to remain constant during the solid integration. For convenience, the index $\varkappa = 0, 1, \dots, \kappa - 1$ is introduced to denote the sub-steps of the solid time integration. Using the position-based Verlet scheme, the deformation tensor, density, and particle position are advanced to the mid-point as

$$\begin{cases} \mathbb{F}_a^{\varkappa+\frac{1}{2}} = \mathbb{F}_a^\varkappa + \frac{1}{2}\Delta t^S \frac{d\mathbb{F}_a}{dt} \\ \rho_a^{\varkappa+\frac{1}{2}} = \rho_a^0 \frac{1}{J} \\ \mathbf{r}_a^{\varkappa+\frac{1}{2}} = \mathbf{r}_a^\varkappa + \frac{1}{2}\Delta t^S \mathbf{v}_a \end{cases}. \quad (34)$$

Then the velocity is updated by

$$\mathbf{v}_a^{\kappa+1} = \mathbf{v}_a^\kappa + \Delta t^S \frac{d\mathbf{v}_a}{dt}. \quad (35)$$

In the final stage, the deformation tensor and position of the solid particles are updated to the next solid time level as

$$\begin{cases} \mathbb{F}_a^{\kappa+1} = \mathbb{F}_a^{\kappa+\frac{1}{2}} + \frac{1}{2} \Delta t^S \frac{d\mathbb{F}_a}{dt} \\ \rho_a^{\kappa+1} = \rho_a^0 \frac{1}{J} \\ \mathbf{r}_a^{\kappa+1} = \mathbf{r}_a^{\kappa+\frac{1}{2}} + \frac{1}{2} \Delta t^S \mathbf{v}_a^{\kappa+1} \end{cases}. \quad (36)$$

Before the next fluid step, the solid time integration described by Eqs. 34–36 is performed for κ sub-steps.

Following Refs. [22, 23], the density is periodically reinitialized to prevent error accumulation from updating the density via the continuity equation in Eq. (18) during long-time simulations. Specifically, the free-surface density initialization scheme of Ref. [24], accounting for solid particles within the support domain, is applied at the beginning of each fluid advection time step as follows:

$$\rho_i = \max \left(\rho_i^*, \rho_i^0 \frac{\sum_j W(\mathbf{r}_{ij}, h^F) + \sum_a W(\mathbf{r}_{ia}, h^F) \frac{V_a^0}{V_i^0}}{\sigma^0} \right), \quad (37)$$

where ρ^* denotes the density before re-initialization, ρ^0 and $\sigma^0 = \sum_j W(\mathbf{r}_{ij}, h^F)$ are the initial density and the reference particle number density, respectively.

For flows without free surface, Eq. (37) is simplified to

$$\rho_i = \rho_i^0 \frac{\sum_j W(\mathbf{r}_{ij}, h^F) + \sum_a W(\mathbf{r}_{ia}, h^F) \frac{V_a^0}{V_i^0}}{\sigma^0} \quad (38)$$

which resets the density using the standard summation formulation [46]. Note that $\frac{V_a^0}{V_i^0}$ is the initial volume ratio between the fluid and solid particle. With $\rho_i^0 = m_i \sigma^0$, we have

$$\rho_i = m_i \sum_j W(\mathbf{r}_{ij}, h^F) + \rho_i^0 \sum_a W(\mathbf{r}_{ia}, h^F) V_a^0. \quad (39)$$

To outline the implementation, the detailed simulation procedure is summarized in Algorithm 1.

3.2. Fluid-shell interaction

Building on the preliminary formulation, the fluid-induced pressure and viscous forces, $\mathbf{f}_a^{F:p}(h^F)$ and $\mathbf{f}_a^{F:v}(h^F)$, also act on shell particle a and contribute to its acceleration. Accordingly, the first conservation equation for the shell is discretized as

$$m_a^0 \frac{d\mathbf{v}_{m,a}}{dt} = \sum_b \left(J_{m,a} \mathbb{N}_a (\mathbb{F}_{m,a})^{-T} \tilde{\mathbb{B}}_a^{0,\mathbf{r}} + J_{m,b} \mathbb{N}_b (\mathbb{F}_{m,b})^{-T} \tilde{\mathbb{B}}_b^{0,\mathbf{r}} \right) \nabla^0 W_{ab} A_a^0 A_b^0 + \mathbf{g} + \mathbf{f}_a^{F:p}(h^F) + \mathbf{f}_a^{F:v}(h^F), \quad (40)$$

where $\tilde{\mathbb{B}}^{0,\mathbf{r}}$ is the correction matrix to remedy the 1st-order inconsistency [42], and A^0 is the initial area of the shell particle. As the imaginary shell particles are introduced to retrieve the kernel completeness, the calculation of $\mathbf{f}_a^{F:p}(h^F)$ and $\mathbf{f}_a^{F:v}(h^F)$ on a shell particle a , and $\mathbf{f}_i^{S:p}(h^F)$ and $\mathbf{f}_i^{S:v}(h^F)$ on a fluid particle i , is needed to be modified accordingly as following sections. Note that only one-sided interaction is considered in this study.

3.2.1. Generation of imaginary shell particles

For a shell particle a located in the support domain of a fluid particle i , i.e., $|\mathbf{r}_{ia}| \leq R^F$ with R^F denoting the cut-off radius of fluid, the imaginary

Algorithm 1: Multi-resolution SPH scheme for FSI problems.

```
1 Setup parameters and initialize the simulation;
2 Compute the initial number density of fluid particles;
3 Compute the surface normal direction of the structure;
4 Obtain the corrected configuration for the solid particles;
5 while the termination condition is not satisfied do
6   Compute the fluid advection time step  $\Delta t_{ad}^F$ ;
7   Reinitialize the fluid density;
8   Update the surface normal direction of the structure;
9   while  $\sum \Delta t_{ac}^F \leq \Delta t_{ad}^F$  do
10    Compute the fluid acoustic time step  $\Delta t_{ac}^F$ ;
11    Integrate the fluid equations using the position-based Verlet
        scheme;
12    Compute the pressure and viscous forces exerted on the
        structure by the fluid;
13    while  $\sum \Delta t^S \leq \Delta t_{ac}^F$  do
14      Compute the solid time step  $\Delta t^S$ ;
15      Integrate the solid equations using the position-based
        Verlet scheme;
16    end
17    Compute the time-averaged velocity and acceleration of the
        solid structure;
18  end
19  Update the particle neighbor list, kernel values, and kernel
        gradients for the fluid particles;
20  Update the particle configuration between the fluid and solid
        particles;
21 end
22 Terminate the simulation;
```

particles of this shell particle a is considered, as shown in Figure 1. The position of k -th imaginary particle is given as:

$$\mathbf{r}_a^k = \mathbf{r}_a + k \cdot dp^S \cdot \mathbf{n}_a, \quad (41)$$

where dp^S is the initial particle spacing of shell, \mathbf{n}_a is the current normal direction of shell particle b , whose orientation is chosen to be consistent with the fluid-to-shell direction.

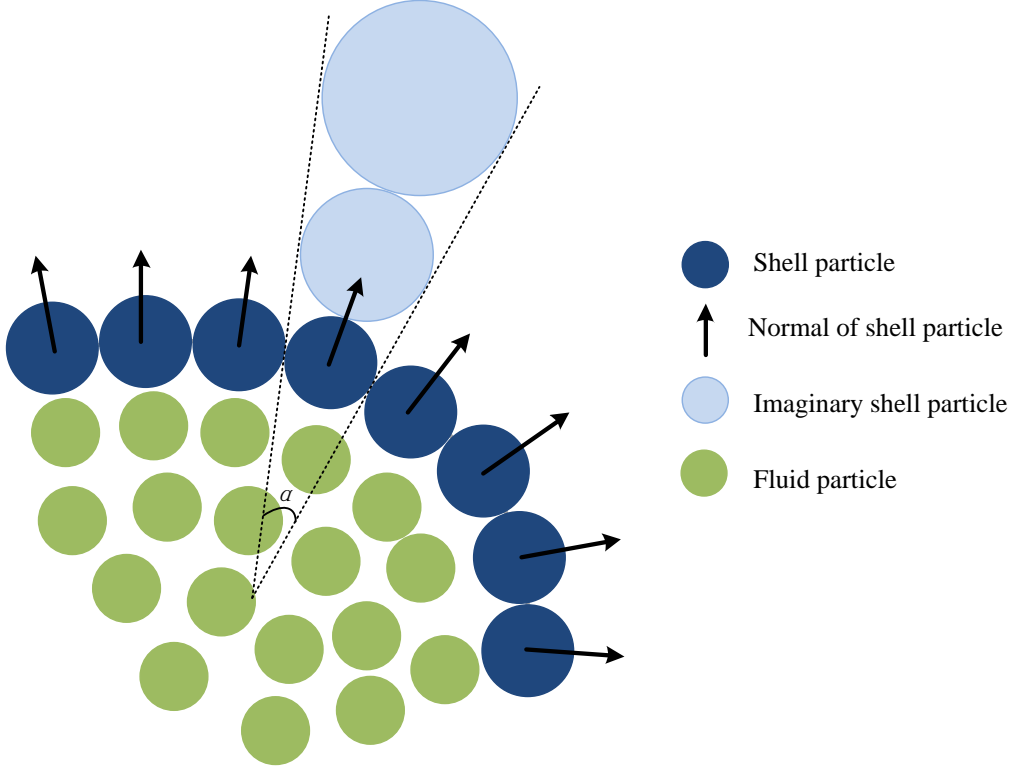


Figure 1: Setup of imaginary shell particles.

The area A_a^k of an imaginary shell particle is determined from the local shell curvature. As shown in Fig. 1, the curvature specifies the center of the local circle in 2D (or the local sphere in 3D). In 2D, two rays drawn from this center through the bounds associated with particle a define the intercepted arc, whose length is taken as A_a^k . In 3D, the corresponding construction defines a spherical surface patch on the local sphere, and its area is taken as

A_a^k . For the 2D case, A_a^k is therefore given by

$$A_a^k = \alpha \left(\frac{1}{\chi_a} + k \cdot dp^S \right), \quad (42)$$

where α is the central angle of the circular sector shown in Figure 1, which can be calculated as

$$\alpha = A_a \cdot \chi_a. \quad (43)$$

Here, χ_a is the principle curvature of particle a , which can be calculated as

$$\chi_a = \nabla \cdot \mathbf{n}_a. \quad (44)$$

Substituting Eq.(43) into Eq.(42), we have:

$$A_a^k = A_a(1 + k \cdot \chi_a \cdot dp^S), \quad (45)$$

For 3D problems, we can calculate the area with two principal curvatures, χ_{a1} and χ_{a2} , and thus the area can be computed as:

$$A_a^k = A_a(1 + k \cdot dp^S \cdot \chi_{a1})(1 + k \cdot dp^S \cdot \chi_{a2}). \quad (46)$$

To get the curvatures χ_{a1} and χ_{a2} , we first calculate the mean curvature M and Gaussian curvature N as

$$M = \chi_{a1} + \chi_{a2} = \frac{1}{2} \nabla \cdot \mathbf{n}_a, \quad (47)$$

$$N = \chi_{a1} \cdot \chi_{a2} = \frac{1}{2} \left[(\nabla \cdot \mathbf{n}_a)^2 - \sum_m \sum_n \left(\frac{\partial n_n}{\partial X_m} \frac{\partial n_m}{\partial X_n} \right) \right], \quad m, n = 1, 2, 3. \quad (48)$$

Then χ_{a1} and χ_{a2} are written as

$$\chi_{a1} = M + \sqrt{M^2 - N}, \quad (49)$$

$$\chi_{a2} = M - \sqrt{M^2 - N}. \quad (50)$$

Note that only if $|\mathbf{r}_{ia}^k| \leq R^F$ and the area A_a^k is positive, the k-th imaginary particle is applied.

3.2.2. Equivalent value of kernel function

Based on the preliminary formulation, the interaction forces are evaluated by Eqs. (22) and (23) for the fluid phase and Eqs. (25) and (26) for the solid phase, while the fluid density initialization is corrected in the presence of solids according to Eq. (37). The introduction of imaginary shell particles can be regarded as modifying the effective kernel quantities used in the above equations, such that the underlying FSI coupling algorithm remains unchanged. The resulting equivalent kernel quantities are denoted by \overline{W}_{ia} , $\frac{\partial \overline{W}_{ia}}{\partial r_{ia}}$, $\frac{\partial \overline{W}_{ai}}{\partial r_{ai}}$, $\overline{\mathbf{e}}_{ia}$, and $\overline{\mathbf{e}}_{ai}$. Note that $\frac{\partial \overline{W}_{ia}}{\partial r_{ia}} = \frac{\partial \overline{W}_{ai}}{\partial r_{ai}}$, and $\overline{\mathbf{e}}_{ia} = -\overline{\mathbf{e}}_{ai}$.

In the density initialization Eq. (38) of fluid with shell interaction, the contribution of a shell particle a is calculated as:

$$\sigma_a = \frac{\overline{W}(\mathbf{r}_{ia}, h^F) V_a^0}{V_i^0} = \frac{\overline{W}(\mathbf{r}_{ia}, h^F) A_a^0 d_a^0}{V_i^0} = \frac{\sum_k W(\mathbf{r}_{ia}^k, h^F) A_a^k dp^S}{V_i^0}, \quad (51)$$

which means the equivalent kernel value $\overline{W}(\mathbf{r}_{ia}, h^F) = \frac{1}{A_a^0 d_a^0} \sum_k W(\mathbf{r}_{ia}^k, h^F) A_a^k dp^S$, considering the effect of imaginary shell particles.

According to Eq. (23), the viscous force $\mathbf{f}_i^{S:p}(h^F)$ acting on a fluid particle i due to the presence of a shell particle a is calculated as

$$\mathbf{f}_{ia}^{S:v}(h^F) = 2\eta V_i \frac{\mathbf{v}_i - \mathbf{v}_a^d}{r_{ia}} \frac{\partial \overline{W}(\mathbf{r}_{ia}, h^F)}{\partial r_{ia}} V_a. \quad (52)$$

While assuming that \mathbf{v}_a^d and r_{ia} are constant for each imaginary particle of shell particle a , Eq. (52) can be written as

$$\mathbf{f}_{ia}^{S:v}(h^F) = 2\eta V_i \frac{\mathbf{v}_i - \mathbf{v}_a^d}{r_{ia}} \sum_k \frac{\partial W(\mathbf{r}_{ia}^k, h^F)}{\partial r_{ia}^k} A_a^k dp^S. \quad (53)$$

Comparing Eqs. (52) and (53), the equivalent kernel value $\frac{\partial \bar{W}(\mathbf{r}_{ia}, h^F)}{\partial r_{ia}}$ is

$$\begin{aligned} \frac{\partial \bar{W}(\mathbf{r}_{ia}, h^F)}{\partial r_{ia}} &= \frac{1}{V_a} \sum_k \frac{\partial W(\mathbf{r}_{ia}^k, h^F)}{\partial r_{ia}^k} A_a^k dp^S \\ &= \frac{1}{A_a} \sum_k \frac{\partial W(\mathbf{r}_{ia}^k, h^F)}{\partial r_{ia}^k} A_a^k. \end{aligned} \quad (54)$$

According to Eq. (22), the pressure force $\mathbf{f}_i^{S:p}(h^F)$ acting on a fluid particle i due to the presence of a shell particle a is calculated as

$$\begin{aligned} \mathbf{f}_{ia}^{S:p}(h^F) &= -2V_i \frac{p_i \rho_a^d + p_a^d \rho_i}{\rho_i + \rho_a^d} \nabla_i \bar{W}(\mathbf{r}_{ia}, h^F) V_a \\ &= -2V_i \frac{p_i \rho_a^d + p_a^d \rho_i}{\rho_i + \rho_a^d} \frac{\partial \bar{W}(\mathbf{r}_{ia}, h^F)}{\partial r_{ia}} \bar{\mathbf{e}}_{ia} V_a. \end{aligned} \quad (55)$$

While assuming that p_a^d is constant for each imaginary particle of shell particle a , Eq. (52) can be written as

$$\mathbf{f}_{ia}^{S:p}(h^F) = -2V_i \frac{p_i \rho_a^d + p_a^d \rho_i}{\rho_i + \rho_a^d} \sum_k \frac{\partial W(\mathbf{r}_{ia}^k, h^F)}{\partial r_{ia}^k} \mathbf{e}_{ia}^k A_a^k dp^S. \quad (56)$$

Comparing Eqs. (55) and (56), and considering Eq. (54), the equivalent value $\bar{\mathbf{e}}_{ia}$ is

$$\bar{\mathbf{e}}_{ia} = \frac{\sum_k \frac{\partial W(\mathbf{r}_{ia}^k, h^F)}{\partial r_{ia}^k} \mathbf{e}_{ia}^k A_a^k}{\sum_k \frac{\partial W(\mathbf{r}_{ia}^k, h^F)}{\partial r_{ia}^k} A_a^k}. \quad (57)$$

3.3. Solid-shell interaction

A particle-to-particle SPH contact model is first formulated for solid–solid interactions by analogy to fluid dynamics, in which interpenetration is prevented. Following the density initialization in Eq. (39), a contact density is introduced for a solid particle i in contact with another solid as

$$\rho_i^c = \rho_i^0 \sum_a W(\mathbf{r}_{ia}, h^c) V_a^0, \quad (58)$$

where the contact smoothing length is defined as $h^c = \frac{h_i^c + h_a^c}{2}$, representing the arithmetic mean of the smoothing lengths of the two contacting solids, The contact particle a is identified as a neighbor in the current configuration but not in the initial configuration, i.e., $r_{ia} \leq R^c$ and $r_{ia}^0 > R^c$.

By analogy to the fluid momentum equation in Eq. (19), the contact interaction is then defined as

$$m_i \frac{d\mathbf{v}_i^c}{dt} = -2 \sum_a V_i V_a \tilde{p}_{ia}^c \nabla_i W_{ia}^{h^c} = -2 \sum_a V_i V_a \tilde{p}_{ia}^c \frac{\partial W(\mathbf{r}_{ia}, h^c)}{\partial r_{ia}^0} \mathbf{e}_{ia}, \quad (59)$$

where $\tilde{p}_{ia}^c = 0.5(p_i^c + p_a^c)$ with $p_i^c = \rho_i^c (c_i^S)^2$ and $p_a^c = \rho_a^c (c_a^S)^2$ denoting the contact pressures. Note that this formulation also takes into account the self-contact dynamics.

For shell-related contact, the Eqs. (58) and (59) are modified as

$$\rho_i^c = \rho_i^0 \sum_a \bar{W}(\mathbf{r}_{ia}, h^c) V_a^0, \quad (60)$$

$$m_i \frac{d\mathbf{v}_i^c}{dt} = -2 \sum_a V_i V_a \tilde{p}_{ia}^c \frac{\partial \bar{W}(\mathbf{r}_{ia}, h^c)}{\partial r_{ia}^0} \bar{\mathbf{e}}_{ia}, \quad (61)$$

where the equivalent values $\bar{W}(\mathbf{r}_{ia}, h^c)$, $\frac{\partial \bar{W}(\mathbf{r}_{ia}, h^c)}{\partial r_{ia}^0}$ and $\bar{\mathbf{e}}_{ia}$ are same with those in section 3.2.2.

4. Numerical examples

In this section, we conduct a series of benchmark tests with available analytical or numerical reference data from the literature to qualitatively and quantitatively assess the accuracy and stability of the proposed framework. Following the validation, we explore the deformation of a complex problem of oil tank car collision to showcase the potential of the present formulation.

The 5th-order Wendland kernel [47], characterized by a smoothing length of $h^S = 1.15dp^S$ and a cut-off radius of $2.3dp^S$, is employed for solid and shell dynamics throughout, while $h^F = 1.3dp^F$ for fluid dynamics.

4.1. Hydrostatic FSI

In this section, the proposed FSI framework is validated using a hydrostatic benchmark test involving a water column resting on an elastic plate. The problem was originally proposed by Fourey et al. [48] and has been widely used to assess the stability and accuracy of FSI solvers [21, 36]. In contrast to previous studies that model the plate as a full-dimensional solid [14, 21, 48], the plate here is represented as a thin shell using the formulation in Section 3 and is coupled to the fluid through the proposed imaginary shell particle approach.

The problem setup is illustrated in Figure 2. A water column with a width of $L = 1.0$ m and an initial height of $H = 2.0$ m is contained in a tank. The bottom of the tank consists of a flexible aluminum plate, while the side walls are rigid. The fluid is modeled as water with a density of $\rho_0^F = 1000.0$ kg/m³ and a gravity of $g = 9.81$ m/s². The aluminum plate has a density of $\rho_0^S = 2700.0$ kg/m³, a Young's modulus of $E = 67.5$ GPa, a Poisson's ratio of $\nu = 0.34$, and a thickness of $d = 0.05$ m. The plate is clamped at both ends. Initially, the system is at rest, and the plate deforms under the hydrostatic pressure of the water column.

The simulation is performed up to $t = 1.0$, s, by which time the initial oscillations have sufficiently damped and the system reaches a quasi-static equilibrium. According to the analytical solution in Ref. [48], the theoretical static mid-span deflection of the plate is -6.85×10^{-5} , m.

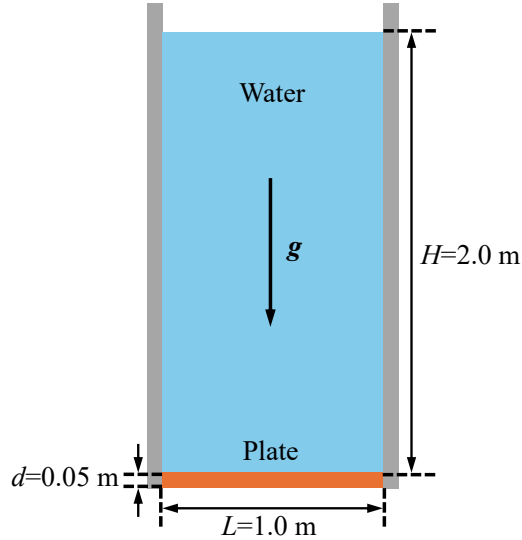


Figure 2: Hydrostatic FSI: Model setup.

Figure 3 shows the pressure field of the water column and the deformation of the shell plate at $t = 0.5$ s. It can be observed that the pressure field exhibits a smooth hydrostatic distribution without non-physical fluctuations near the fluid-shell interface. This demonstrates that the proposed imaginary shell particle method effectively completes the kernel support for fluid particles near the boundary, preventing particle penetration and ensuring correct pressure transmission. Simultaneously, the von Mises stress distribution on the shell particles also exhibits a smooth pattern without introducing any numerical instabilities.

The time history of the vertical displacement at the mid-span of the plate is plotted in Figure 4. The result shows that the plate oscillates initially and gradually converges to a stable value. Three different particle resolutions ($dp = dp^F = dp^S = d/2, d/4$ and $d/8$) are examined to assess the convergence behavior of the method. With the increase of resolution, the oscillation

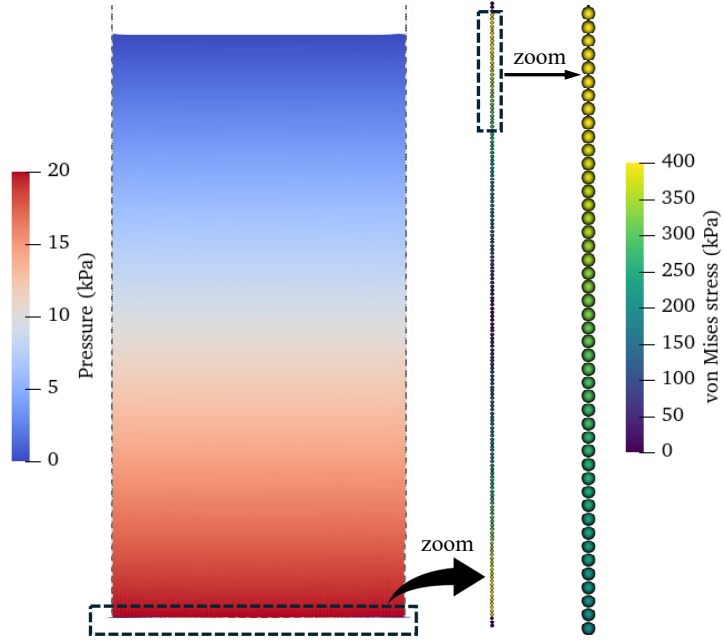


Figure 3: Hydrostatic FSI: The pressure distribution of the water column and the plate particles colored by von Mises stress.

amplitude decreases, and the converged displacement approaches the analytical solution. The converged displacement obtained by the present shell-based SPH method agrees very well with the analytical solution (-6.85×10^{-5} m) and the numerical results from solid-based SPH solvers [21]. This validates that the proposed framework can accurately capture the hydro-elastic response, proving that the reduced-dimensional shell model along with the projection method, effectively mimics the behavior of a full-dimensional solid boundary in hydrostatic FSI scenarios.

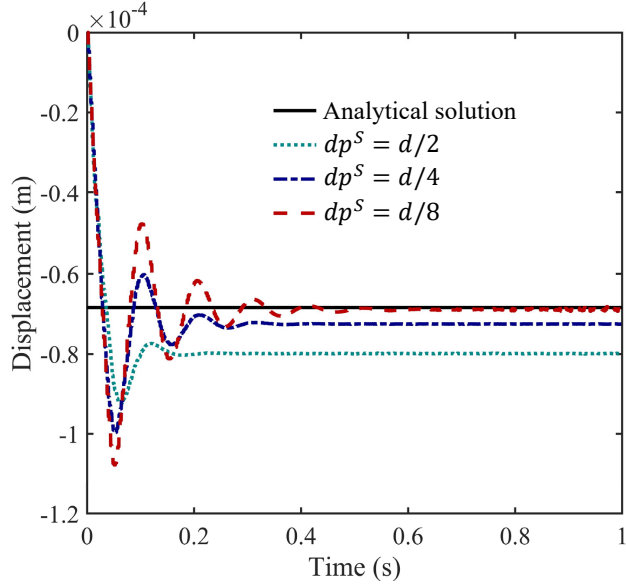


Figure 4: Hydrostatic FSI: Time history of the vertical mid-span displacement of the elastic plate.

4.2. Dam-break flow through an elastic gate

To further evaluate the performance of the proposed framework in handling free-surface flows interacting with thin flexible structures, the benchmark problem of a dam-break flow through an elastic gate is simulated. This problem was originally investigated experimentally by Antoci et al. [11] and has been widely adopted as a standard validation case for various FSI solvers [14, 21, 48]. It is important to note that in these reference studies, the elastic gate was typically modeled using solid-based discretization methods, such as multi-layer SPH solid particles [14, 21] or solid finite elements [48]. In contrast, the present work utilizes the proposed shell formulation represented by a single layer of particles to model the gate, which significantly reduces the computational cost because of less particles while maintaining accuracy.

The computational setup is illustrated in Figure 5. A tank contains a water column with an initial height of 0.14 m and a width of 0.1 m. An elastic gate, acting as a dam, is clamped at its upper end to a rigid wall, while its lower end is free to move. The gate has a height of 0.079 m and a thickness of $d = 0.005$ m. The fluid is modeled as water with a density of $\rho_0^F = 1000.0 \text{ kg/m}^3$. The elastic gate is made of rubber with a density of $\rho_0^S = 1100.0 \text{ kg/m}^3$, a Young's modulus of $E = 7.8 \text{ MPa}$, and a Poisson's ratio of $\nu = 0.47$.

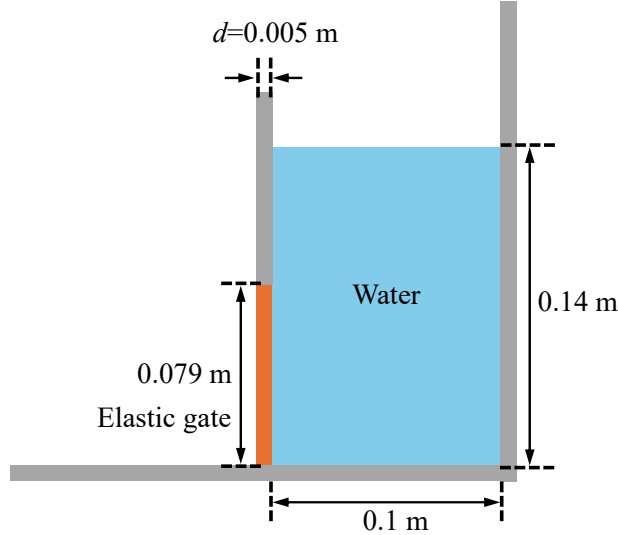


Figure 5: Dam-break flow through an elastic gate: Initial configuration and geometric parameters.

At $t = 0$ s, the water column is released under gravity ($g = 9.81 \text{ m/s}^2$). The hydrostatic pressure acts on the elastic gate, inducing significant non-linear deformation and allowing the water to flow underneath. Figure 6 presents snapshots of the simulation at representative time instants. The fluid domain is colored by horizontal velocity, while the shell particles are

colored by the von Mises stress. Qualitatively, the predicted deformation profiles of the gate and the flow patterns show strong agreement with the experimental observations by Antoci et al. [11].

To quantitatively validate the accuracy and convergence of the shell-based approach, the horizontal and vertical displacements of the gate’s free end are monitored. A convergence study is conducted using three different particle resolutions: $dp = dp^F = dp^S = d/4$, $d/8$, and $d/16$, where d is the thickness of the elastic gate. The time histories of the tip displacements are plotted in Figure 7. A clear convergence trend is evident: as the particle resolution increases, the difference between the results of adjacent resolutions (i.e., between $d/4$ and $d/8$, and between $d/8$ and $d/16$) progressively diminishes, indicating that the solution is approaching a resolution-independent state.

Furthermore, the trade of the displacement curves exhibit good agreement with both the experimental data [11] and the numerical results from the enhanced ISPH-SPH method [14]. It is observed that some deviations exist between the simulation and the experiment during the closing phase of the gate (the rebound period). Consistent with findings in literature [21, 17, 14, 49], these discrepancies are likely attributed to the simplified material model employed in the simulation [49], which may not fully capture the complex hysteretic damping properties of the actual rubber material used in the experiment. Despite this, the proposed fluid-shell coupling framework proves capable of reproducing the dominant physics of FSI scenarios with accuracy comparable to fluid-solid models.

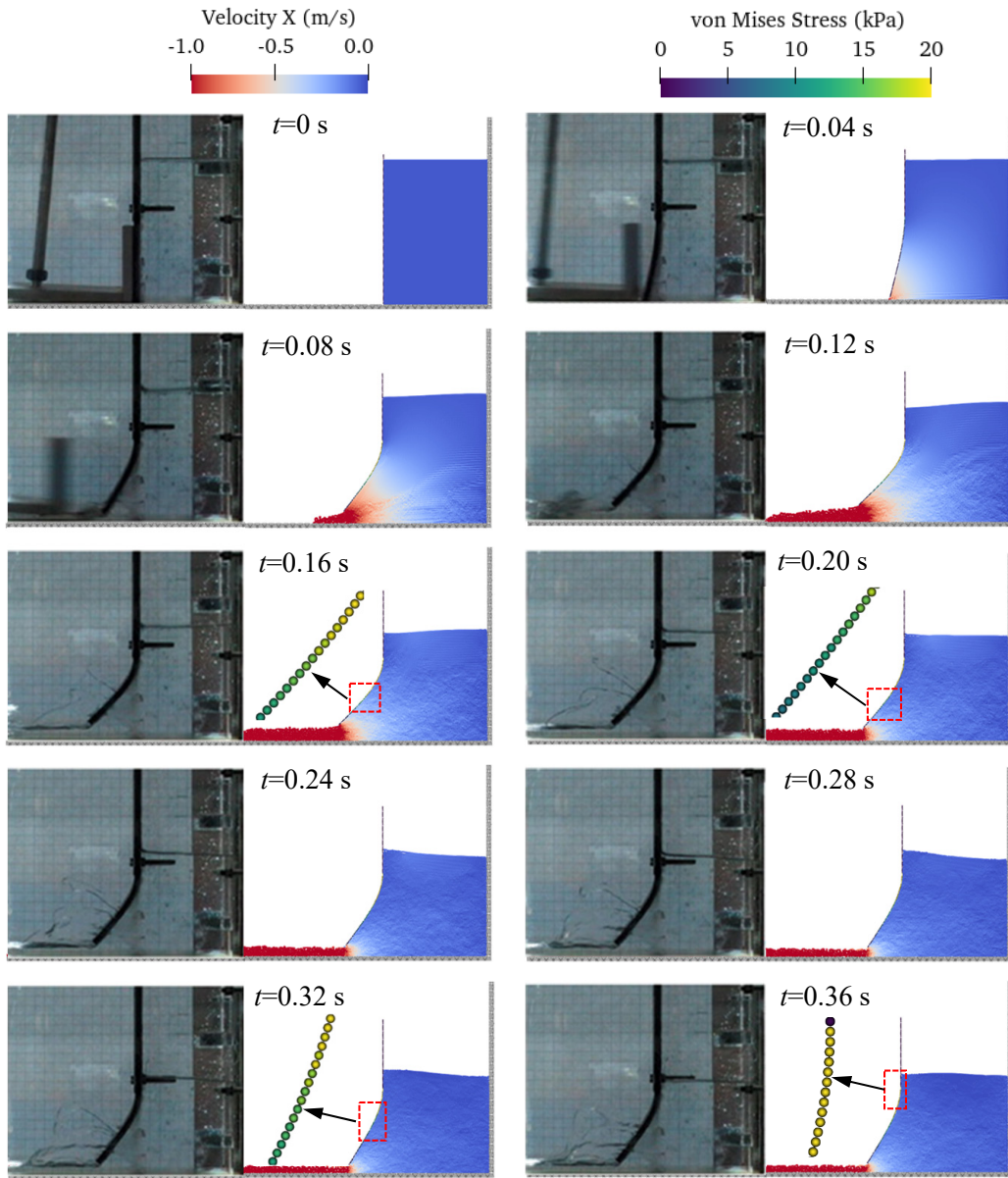


Figure 6: Dam-break flow through an elastic gate: Snapshots of the fluid velocity field and the von Mises stress distribution on the shell structure at different time instants. The deformed shapes are compared with the experimental profiles from Antoci et al. [11].

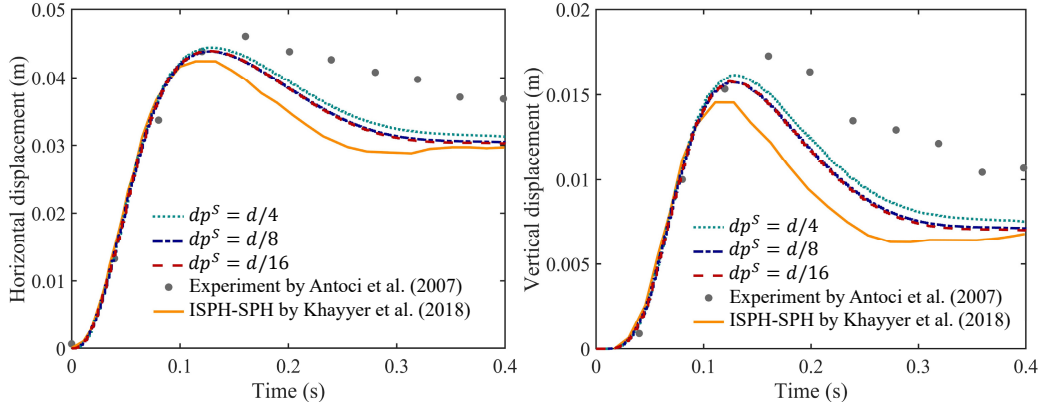


Figure 7: Dam-break flow through an elastic gate: Time histories of the horizontal (left) and vertical (right) displacements of the free end of the gate. The present results with three resolutions ($dp = d/4, d/8, d/16$) are compared with the experimental data of Antoci et al. [11] and the numerical results of Khayyer et al. [14].

4.3. Dam-break impact on an elastic plate

To rigorously validate the proposed FSI framework for hydroelastic problems involving violent free-surface flows and large structural deformations, the benchmark case of a 3D dam-break flow impacting an elastic plate is simulated. The numerical setup faithfully reproduces the experimental configuration conducted by Liao et al. [50], and the results are compared with both experimental data and numerical results from previous studies [16, 10, 51].

The geometric setup is shown in Fig. 8. A water column is initially confined in a tank by a vertical gate. Downstream of the water column, a vertical elastic plate is installed and clamped at the tank bottom. In this study, the case with an initial water height of $H = 0.2, \text{m}$ is considered for validation. The plate is made of rubber with density $\rho_0 = 1164.0, \text{kg/m}^3$, Young's modulus $E = 3.5, \text{MPa}$, and Poisson's ratio $\nu = 0.49$, and has a

thickness of $d = 0.004$, m. To quantify the structural response, the horizontal displacement is recorded at a marker on the plate centerline located 0.0875 , m above the bottom, consistent with the experimental measurement point in Ref. [50].

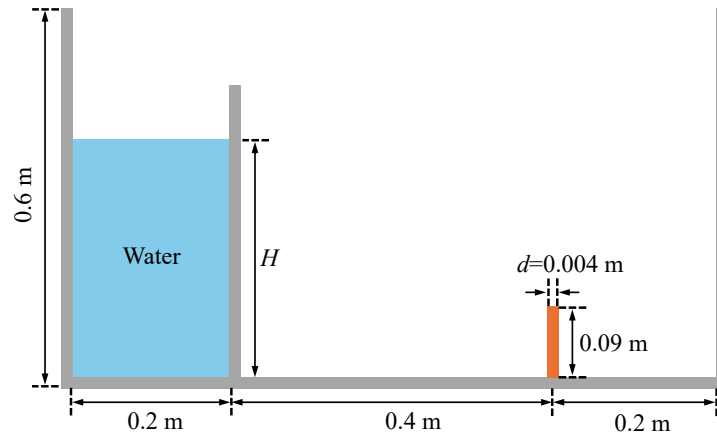


Figure 8: Dam-break flow impacts an elastic plate: 2D schematic diagram of the FSI dam-breaking test setup. The 3D geometry has an identical cross-section with a width of 0.2 m.

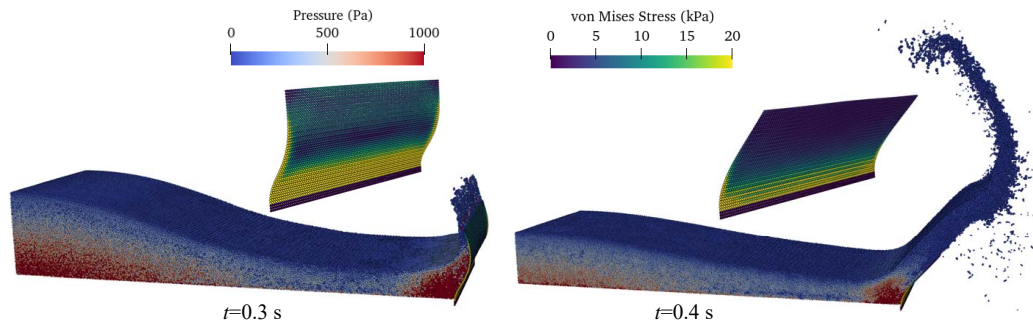


Figure 9: Dam-break flow impacts an elastic plate: 3D SPH simulation snapshots showing the fluid distribution and structural deformation at $t = 0.3$ s and $t = 0.4$ s.

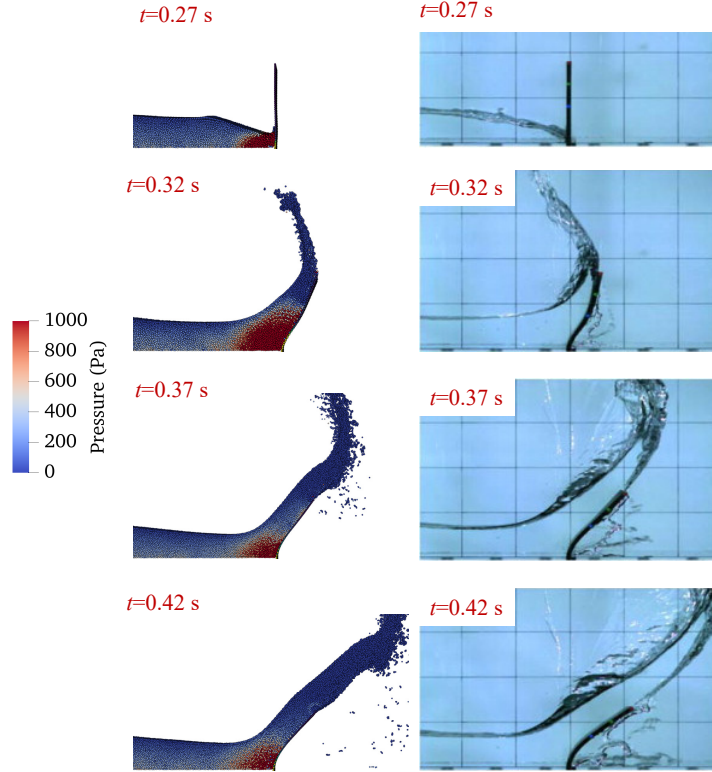


Figure 10: Dam-break flow impacts an elastic plate: Comparison between the present SPH results and experimental results [50] at four typical time instants.

As highlighted by Sun et al. [16], the kinematics of the gate removal plays a critical role in the early development of the flow and the subsequent impact forces. To minimize discrepancies arising from the instant removal assumption, the gate motion in the SPH simulation is prescribed using the following polynomial law derived from experimental observations [16]:

$$h_g(t) = -285.115t^3 + 72.305t^2 + 0.1463t, \quad (62)$$

where $h_g(t)$ denotes the vertical position of the gate. The simulation is conducted over a physical duration of $t = 0.5, \text{s}$. As reported in Ref. [16],

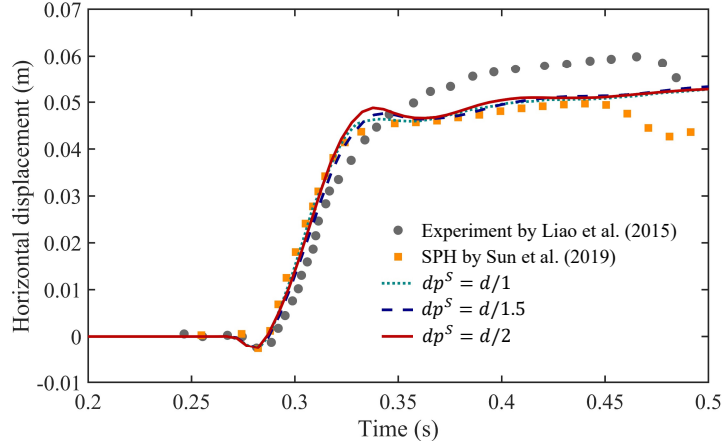


Figure 11: Dam-break flow impacts an elastic plate: Time history of the horizontal displacements on the elastic plate for the case with an initial water depth of $H = 0.2$, m under three spatial particle discretization. The SPH results are compared with the experimental data from Ref. [50] and SPH result from Ref. [16].

single-phase simulations typically start to deviate from the experimental measurements beyond this time because an air cavity becomes entrapped behind the plate. The resulting air-cushion effect markedly affects the rebound dynamics and would require a multiphase air–water–structure model, which is beyond the scope of the present study.

Figure 9 illustrates the 3D spatiotemporal evolution of the water-plate interaction. The proposed framework successfully captures the complex flow features, including the run-up, splashing, and the interplay between fluid loading and structural deformation. Specifically, at $t = 0.3$ s, the impinging flow surges upward upon contact with the barrier. The plate responds with a synchronized deformation, adopting a characteristic "S-shaped" profile. This deformation mode occurs because the hydrodynamic impact momentum is primarily concentrated on the lower-central region of the structure at this

stage. Subsequently, by $t = 0.4$ s, the fluid is guided upward along the deflecting structure, generating significant splashing. As the hydrodynamic loading redistributes to the upper portion of the plate, the deformation mode transitions into a uniform arc shape.

A qualitative comparison is presented in Figure 10, where the numerical snapshots are aligned with experimental photographs [50] at four typical time instants. The SPH results show good agreement with the experiment in terms of the free surface profile and the structural deflection. To further assess the accuracy and convergence of the method, a spatial resolution study is conducted using three different particle spacings: $dp = dp^F = dp^S = d$, $d/1.5$, and $d/2$, where d is the plate thickness. The time histories of the horizontal displacement at the marker point are plotted in Figure 11. The results align well with both the experimental data [50] and the reference numerical solution [16]. This confirms the capability of the proposed multi-resolution framework to accurately predict the fluid-structure interaction dynamics in 3D space.

4.4. Flow around cylinder

To evaluate the capability in capturing unsteady wake dynamics, we consider the canonical benchmark of two-dimensional laminar flow past a circular cylinder. In the present study, the cylinder is modeled as a rigid shell structure interacting with the surrounding fluid. The simulation is conducted at a Reynolds number of $Re = \rho_\infty U_\infty D / \mu = 100$. The fluid density and velocity in the far-field are set to $\rho_\infty = 1.0$ and $U_\infty = 1.0$, and the cylinder diameter $D = 2.0$. To minimize boundary effects, a rectangular computational domain of size $[25D, 15D]$ is employed, with the cylinder center located at

$(7.5D, 7.5D)$. Periodic boundary conditions are applied to both the stream-wise (left-right) and transverse (top-bottom) boundaries. The simulation is integrated up to a final physical time of $t = 300$ to ensure a fully developed periodic flow state. The model setup, highlighting the shell-based representation of the cylinder, is illustrated in Figure 12.

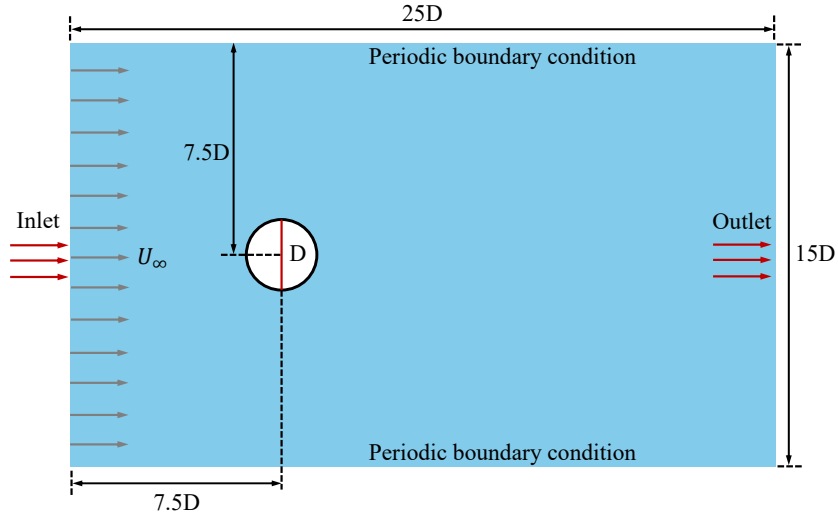


Figure 12: Flow around cylinder: Model setup.

The hydrodynamic forces acting on the cylinder are quantified using the drag (C_D) and lift (C_L) coefficients, defined as:

$$C_D = \frac{F_D}{\frac{1}{2}\rho_\infty U_\infty^2 D}, \quad C_L = \frac{F_L}{\frac{1}{2}\rho_\infty U_\infty^2 D}, \quad (63)$$

where F_D and F_L represent the total fluid forces in the streamwise and transverse directions, respectively. The periodicity of the wake is characterized by the Strouhal number, $St = fDU_\infty^{-1}$, where f denotes the vortex shedding frequency derived from the spectral analysis of the lift coefficient.

Figure 13 visualizes the velocity magnitude field at representative instants. The results distinctively capture the shear layer separation from the

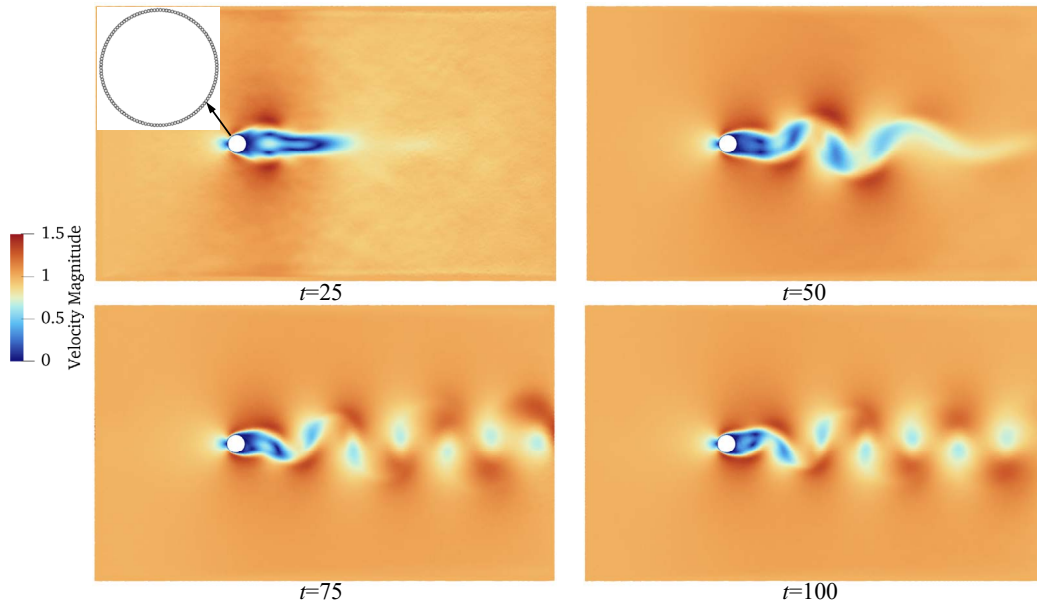


Figure 13: Flow around cylinder: Velocity contour at different time instants. $Re = 100$ and $dp = 0.05$.

cylinder surface and the subsequent formation of the von Kármán vortex street, characterized by the alternating shedding of counter-rotating vortices downstream.

The temporal evolution of the coefficients is presented in Figure 14. Following the initial transient phase, the flow settles into a stable periodic regime where C_L oscillates symmetrically around zero, and C_D fluctuates around a mean value. The convergence of these results is verified across different particle resolutions. Table 1 provides a quantitative comparison of the mean drag coefficient, lift amplitude, and Strouhal number against established benchmarks. At the finest resolution ($dp = 0.025$), we obtained a mean C_D of 1.59 and an St of 0.179. While slightly higher than values from grid-based Eulerian methods (e.g., Brehm et al. [53]), our results show excellent agreement

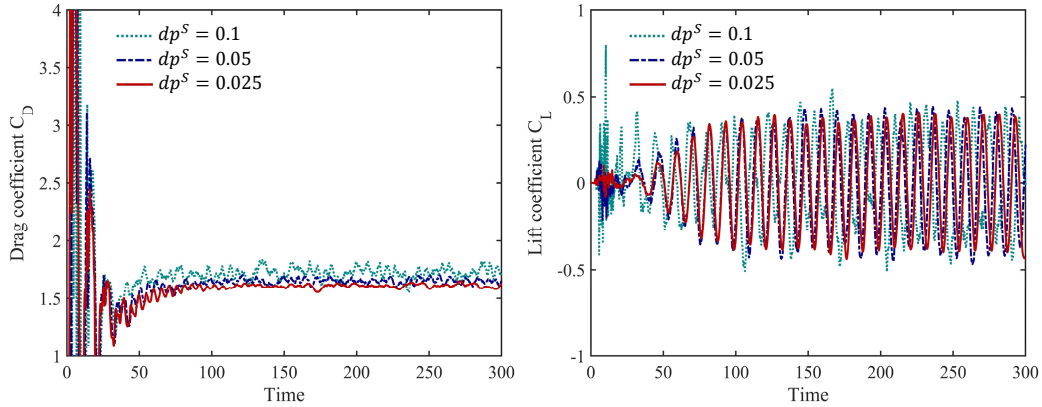


Figure 14: Flow around a cylinder: Drag (left panel) and lift (right panel) coefficients with the time for different particle resolutions ($Re = 100$).

with recent Lagrangian SPH studies, such as those by Zhang et al. [58]. It is noteworthy that considerable scatter in force coefficients has been extensively documented in the literature for flows at moderate Reynolds numbers, suggesting a high sensitivity to numerical configurations or the potential existence of multiple realizable solutions [58]. Consequently, the deviations observed in the present study are not unexpected.

4.5. Block sliding

To validate the accuracy of the proposed contact algorithm, specifically between an elastic solid and a shell structure, the block sliding benchmark is conducted [59]. The geometric configuration of the problem is depicted in Fig. 15. An elastic cube with a side length of 1 m is positioned on an inclined plane with a tilt angle of $\theta = 10^\circ$. A distinguishing feature of this test, compared to standard rigid-wall boundary treatments (e.g., in Ref. [59]), is that the fixed wall is modeled here using a single-layer shell formulation. This setup rigorously tests the capability of the contact forcing to prevent

Table 1: Flow around a cylinder: Comparison of drag and lift coefficients and Strouhal number with reference data at $Re = 100$ and $dp = 0.025$.

	C_D	C_L	St
White [52]	1.46	–	–
Brehm et al. [53]	1.32 ± 0.0100	± 0.320	0.165
Al-Marouf and Samtaney [54]	1.34 ± 0.0089	± 0.325	0.166
Liu et al. [55]	1.35 ± 0.0120	± 0.339	0.165
Le et al. [56]	1.37 ± 0.0090	± 0.323	0.160
Russell and Wang [57]	1.38 ± 0.0070	± 0.300	0.172
Zhang et al. [58]	1.61 ± 0.0050	± 0.448	0.171
Present	1.59 ± 0.0226	± 0.421	0.179

penetration while maintaining the correct sliding mechanics.

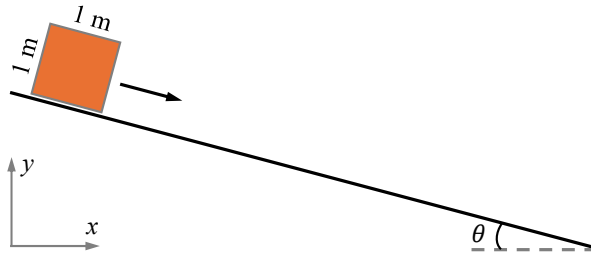


Figure 15: Block sliding: Model setup.

The material properties of the elastic block are set as follows: density $\rho = 1000 \text{ kg/m}^3$, Young's modulus $E = 1.0 \times 10^5 \text{ Pa}$, and Poisson's ratio $\nu = 0.45$. The system is driven solely by a gravitational acceleration of $g = 9.8 \text{ m/s}^2$. The initial particle spacing is set as $dp = 0.05 \text{ m}$. Assuming a frictionless interface between the elastic block and the shell boundary, the theoretical

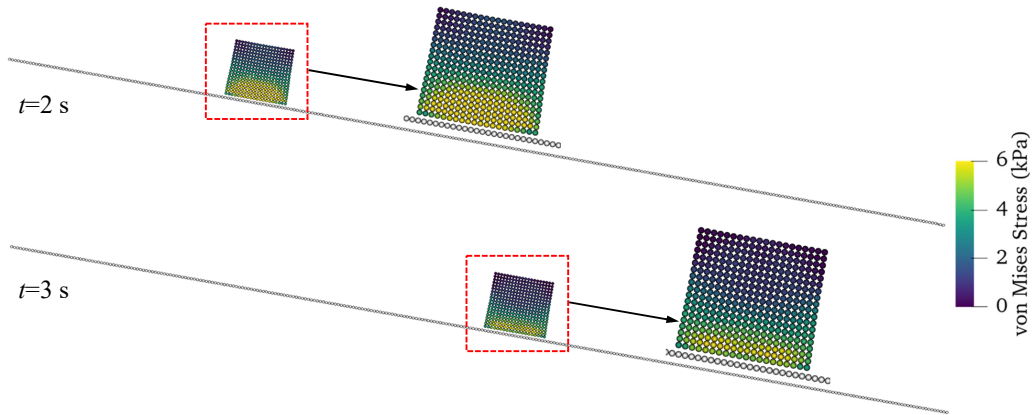


Figure 16: Block sliding: SPH simulation snapshots at $t = 2$ s and $t = 3$ s.

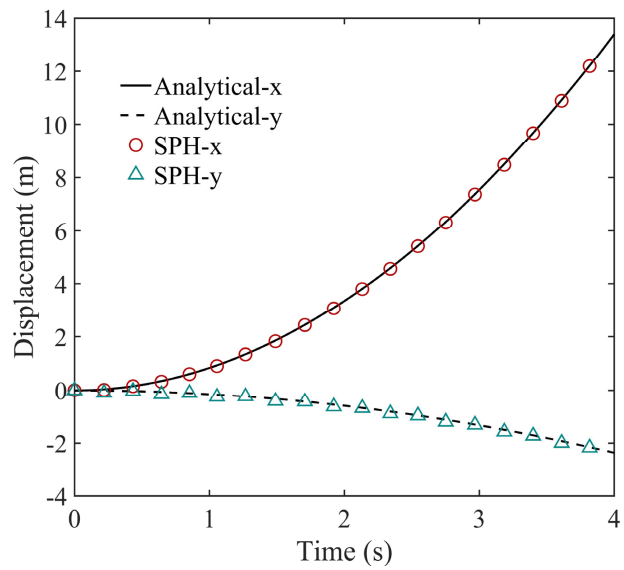


Figure 17: Block sliding: Time history of the block center displacement in the x - and y -directions.

trajectory of the block center of mass can be derived from Newton's laws of

motion:

$$\begin{aligned} x(t) &= x_0 + \frac{1}{2}g \sin \theta \cos \theta t^2, \\ y(t) &= y_0 - \frac{1}{2}g \sin^2 \theta t^2, \end{aligned} \tag{64}$$

where x_0 and y_0 represent the initial coordinates.

Fig. 16 presents the simulation snapshots at $t = 2$ s and $t = 3$ s. Qualitatively, the elastic block maintains its geometric integrity throughout the sliding process. Crucially, the interaction between the solid particles and the underlying shell particles remains stable, with no unphysical penetration or separation observed at the interface.

For a quantitative assessment, the time evolution of the block’s displacement is analyzed. Fig. 17 compares the numerical results against the analytical solution given in Eq. (64). The SPH-predicted displacements in both the horizontal (x) and vertical (y) directions exhibit excellent agreement with the theoretical curves. These results confirm that the proposed method effectively captures the dynamic contact behavior between elastic bodies and shell-based boundaries.

4.6. Three rings contact

The solid-shell, shell-shell and shell-self contacts of three rings is designed to further evaluate the performance of the proposed framework following Ref. [60]. The initial configuration for this problem is shown in Figure 18. The dimensions of the rings are as follows: the inner and outer diameters of the largest ring are 26 and 30, respectively. For the medium-sized ring, these diameters are 10 and 12, while the smallest ring has inner and outer diameters of 8 and 10. The center of the largest ring is located at $(0, 0)^T$, the center of the medium-sized ring is at $(3.95, -3.95)^T$, and the smallest

ring is at $(-3.95, 4.25)^T$. The three rings are modeled with Young's moduli $E_1 = 10,000$ for the smallest ring, $E_2 = 2250$ for the medium ring, and $E_3 = 288,000$ for the largest ring. The Poisson's ratio is $\nu = 0.125$ for all rings, and the initial densities are $\rho_1 = 0.1$, $\rho_2 = 0.01$, and $\rho_3 = 1.0$ for the smallest, medium, and largest rings, respectively.

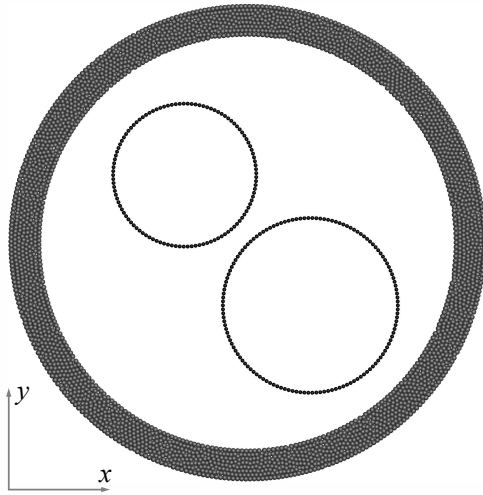


Figure 18: Three rings contact: Initial configuration.

The external boundary of the largest ring is fixed, while the smallest ring, positioned inside the largest and adjacent to a third medium-sized ring, is initially given a velocity of $\mathbf{v} = (30.0, -30.0)^T$. As the smallest ring collides with the medium-sized ring, both rings move together toward the inner surface of the largest ring. During this process, self-contact occurs within the medium-sized ring, as illustrated in the deformed configurations in Figure 19. As shown in the results, the framework efficiently handles the large deformations and contact that occur during the impact, accurately identifying self-contact regions, capturing the complex dynamics of the interacting rings,

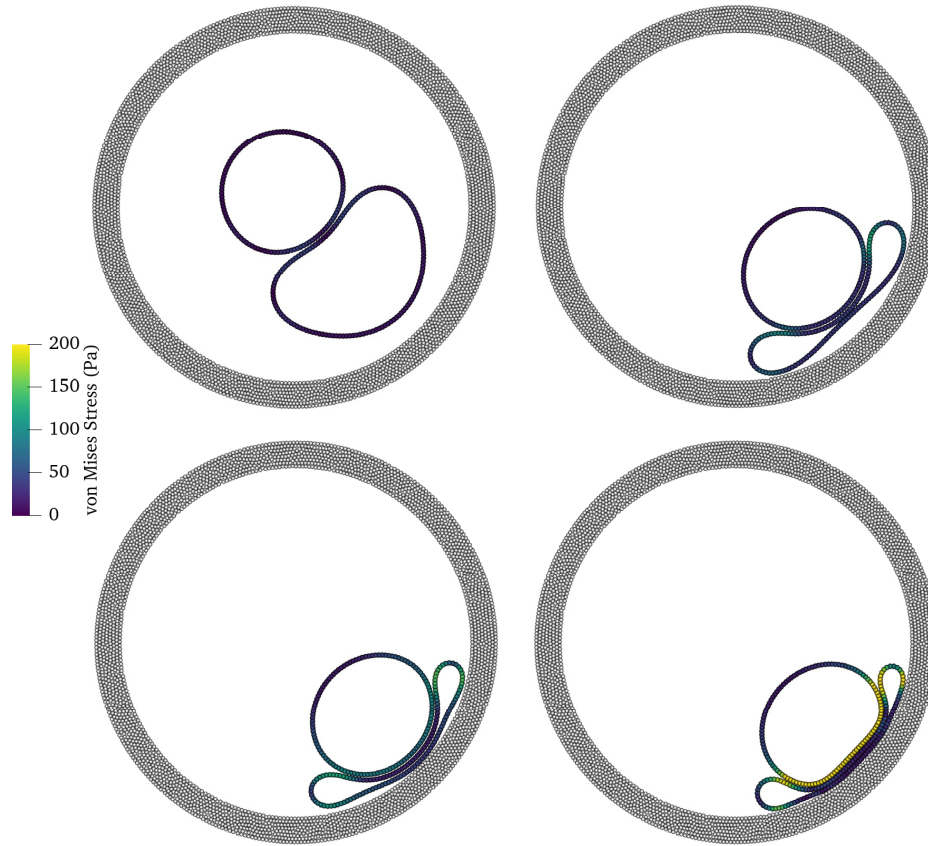


Figure 19: Three rings contact: Deformed configurations colored by von Mises stress at several temporal instants.

and aligning well with the findings presented in Ref. [60] (refer to Figure 16 in their work).

4.7. Oil tank collision

In this section, we present a collision simulation of a oil tank car impacted by a truck at a level crossing following Ref. [61], to analyze the stress distribution and displacement behavior of the tank car during the collision. As shown in Figure 20, the oil tank car is treated by shell model with a

thickness of $d = 0.011$ m, a density of $\rho_0^S = 7850.0$ kg/m³, an elastic modulus of $E = 206.0$ GPa, and a Poisson’s ratio of $\nu = 0.28$. The tank car is half-filled by oil, whose material properties are: a density of $\rho_0^F = 700.0$ kg/m³, a dynamic viscosity of $\mu = 0.1$ Pa·s. The truck is moving at 20 m/s, colliding with the middle of the tank. As shown in Figure 21, the deformation of tank is well captured, and the stress of tank and the pressure of oil are smooth.



Figure 20: Oil tank collision: Initial configuration.

In this section, we present a collision simulation of an oil tank car impacted by a truck at a level crossing, following Ref. [61], to analyze the stress distribution and displacement behavior of the tank car during the collision. As depicted in Figure 20, the oil tank car is modeled using a layer of shell particles with a thickness of $d = 0.011$, m, a density of $\rho_0^S = 7850$, kg/m³, an elastic modulus of $E = 206$, GPa, and a Poisson’s ratio of $\nu = 0.28$. The tank is half-filled with oil, characterized by a density of $\rho_0^F = 700$, kg/m³ and a dynamic viscosity of $\mu = 0.1$, Pa·s. The truck, traveling at 20 m/s, collides with the center of the tank. As shown in Fig. 21, the proposed framework accurately captures the tank deformation at several representative time instants. Despite the strongly coupled and highly dynamic setting involving

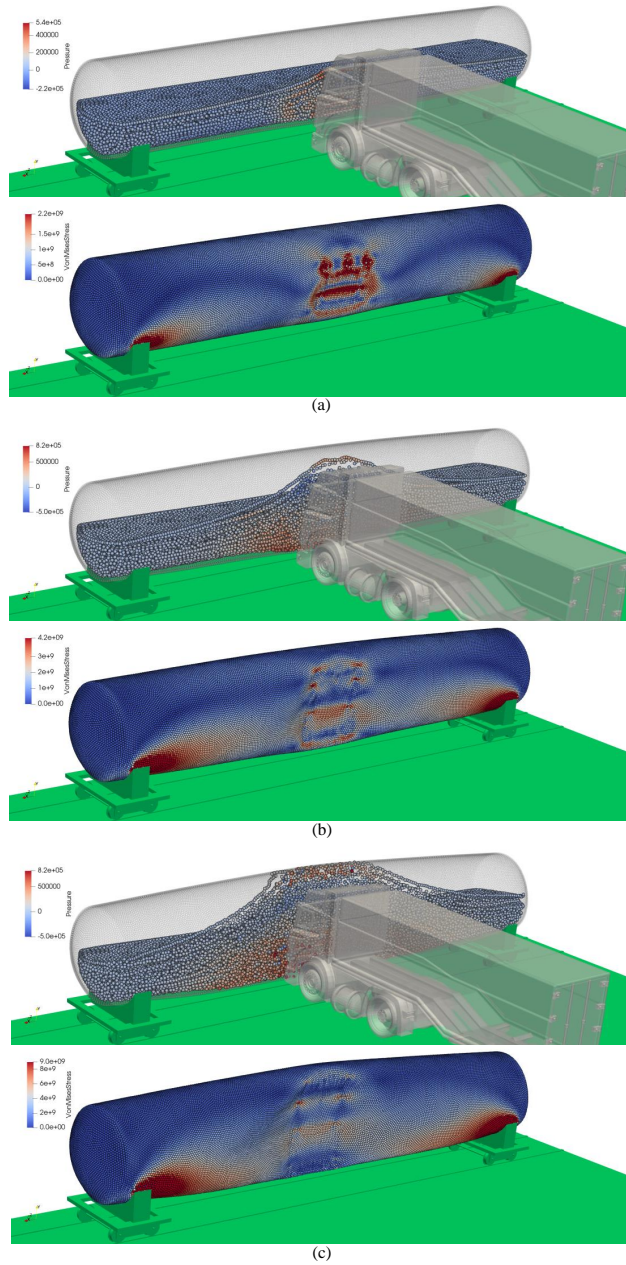


Figure 21: Oil tank collision: Deformed configurations colored by pressure and von Mises stress at several temporal instants.

large deformation, fluid motion, and contact events, the stress field in the tank and the oil pressure remain smooth and free of spurious oscillations. These results demonstrate the capability of the proposed framework to handle complex interaction scenarios in an industrially relevant setting.

5. Concluding remarks

In this study, we have proposed a unified Smoothed Particle Hydrodynamics (SPH) framework for simulating shell-related interactions, including one-sided fluid-shell, solid-shell, shell-shell, and shell-self contact dynamics. A key contribution of this work is the introduction of imaginary shell contact particles, projected from real shell particles along the normal direction, which effectively transforms the reduced-dimensional shell model into a full-dimensional one. This projection method not only ensures kernel completeness in fluid-shell interactions but also extends the developed solid contact models to accurately handle complex shell-related contact scenarios. The developed framework has been validated through a series of benchmark tests, and the results show that the proposed method can effectively simulate challenging scenarios involving shell structures and multiple types of interactions with reliable performance.

While the proposed framework provides a robust foundation for shell-related interaction modeling, further extensions are possible. A natural next step is to extend the formulation to support two-sided fluid-shell interactions, in which the shell is coupled to fluids on both sides.

CRedit authorship contribution statement

D. Wu: Conceptualization, Methodology, Investigation, Visualization, Validation, Formal analysis, Writing - original draft, Writing - review and editing; **S.H. Zhang:** Visualization, Validation, Writing - original draft, Writing - review and editing; **W.Y. Kong:** Methodology, Investigation, Validation; **X.Y. Hu:** Supervision, Methodology, Investigation, Writing - review and editing.

Declaration of competing interest

The authors declare that they have no known competing financial interests or personal relationships that could have appeared to influence the work reported in this paper.

Acknowledgments

D. Wu and X.Y. Hu would like to express their gratitude to the German Research Foundation (DFG) for their sponsorship of this research under grant number DFG HU1527/12-4.

References

- [1] P. Randles, L. D. Libersky, Smoothed particle hydrodynamics: some recent improvements and applications, *Computer Methods in Applied Mechanics and Engineering* 139 (1-4) (1996) 375–408.
- [2] M. Luo, A. Khayyer, P. Lin, Particle methods in ocean and coastal engineering, *Applied Ocean Research* 114 (2021) 102734.
- [3] C. Zhang, Y.-j. Zhu, D. Wu, N. A. Adams, X. Hu, Smoothed particle hydrodynamics: Methodology development and recent achievement, *Journal of Hydrodynamics* 34 (5) (2022) 767–805.
- [4] F. Xu, J. Wang, Y. Yang, L. Wang, Z. Dai, R. Han, On methodology and application of smoothed particle hydrodynamics in fluid, solid and biomechanics, *Acta Mechanica Sinica* 39 (2) (2023) 722185.
- [5] A. Khayyer, D. Violeau, S. Shao, D. Durante, Preface: Latest advances in sph for fluid mechanics, *European Journal of Mechanics B Fluids* 98 (2023) 208–210.
- [6] J. J. Monaghan, Smoothed particle hydrodynamics, *Reports on Progress in Physics* 68 (8) (2005) 1703.
- [7] M. Liu, G. Liu, Smoothed particle hydrodynamics (SPH): an overview and recent developments, *Archives of Computational Methods in Engineering* 17 (1) (2010) 25–76.
- [8] J. J. Monaghan, Smoothed particle hydrodynamics and its diverse applications, *Annual Review of Fluid Mechanics* 44 (2012) 323–346.

- [9] C. Zhang, M. Rezavand, Y. Zhu, Y. Yu, D. Wu, W. Zhang, J. Wang, X. Hu, SPHinXsys: An open-source multi-physics and multi-resolution library based on smoothed particle hydrodynamics, *Computer Physics Communications* (2021) 108066.
- [10] P.-N. Sun, D. Le Touze, G. Oger, A.-M. Zhang, An accurate FSI-SPH modeling of challenging fluid-structure interaction problems in two and three dimensions, *Ocean Engineering* 221 (2021) 108552.
- [11] C. Antoci, M. Gallati, S. Sibilla, Numerical simulation of fluid–structure interaction by SPH, *Computers & Structures* 85 (11-14) (2007) 879–890.
- [12] A. Rafiee, K. P. Thiagarajan, An SPH projection method for simulating fluid-hypoelastic structure interaction, *Computer Methods in Applied Mechanics and Engineering* 198 (33-36) (2009) 2785–2795.
- [13] L. Han, X. Hu, SPH modeling of fluid-structure interaction, *Journal of Hydrodynamics* 30 (1) (2018) 62–69.
- [14] A. Khayyer, H. Gotoh, H. Falahaty, Y. Shimizu, An enhanced ISPH–SPH coupled method for simulation of incompressible fluid–elastic structure interactions, *Computer Physics Communications* 232 (2018) 139–164.
- [15] M. Liu, Z. Zhang, Smoothed particle hydrodynamics (SPH) for modeling fluid-structure interactions, *Science China Physics, Mechanics & Astronomy* 62 (8) (2019) 1–38.
- [16] P. Sun, D. Le Touzé, A.-M. Zhang, Study of a complex fluid-structure dam-breaking benchmark problem using a multi-phase SPH method

- with APR, *Engineering Analysis with Boundary Elements* 104 (2019) 240–258.
- [17] Z. Zhang, T. Long, J. Chang, M. Liu, A smoothed particle element method (SPEM) for modeling fluid–structure interaction problems with large fluid deformations, *Computer Methods in Applied Mechanics and Engineering* 356 (2019) 261–293.
- [18] J. M. Pearl, C. D. Raskin, J. M. Owen, SPH formulation and fluid-solid interface model for the fully compressible interaction of dissimilar materials, Tech. rep., Lawrence Livermore National Lab.(LLNL), Livermore, CA (United States) (2021).
- [19] A. Khayyer, H. Gotoh, Y. Shimizu, T. Gotoh, An improved Riemann SPH-Hamiltonian SPH coupled solver for hydroelastic fluid-structure interactions, *Engineering Analysis with Boundary Elements* 158 (2024) 332–355.
- [20] S. Adami, X. Hu, N. A. Adams, A generalized wall boundary condition for smoothed particle hydrodynamics, *Journal of Computational Physics* 231 (21) (2012) 7057–7075.
- [21] C. Zhang, M. Rezavand, X. Hu, A multi-resolution SPH method for fluid-structure interactions, *Journal of Computational Physics* 429 (2021) 110028.
- [22] A. Colagrossi, M. Landrini, Numerical simulation of interfacial flows by smoothed particle hydrodynamics, *Journal of Computational Physics* 191 (2) (2003) 448–475.

- [23] C. Zhang, X. Y. Hu, N. A. Adams, A generalized transport-velocity formulation for smoothed particle hydrodynamics, *Journal of Computational Physics* 337 (2017) 216–232.
- [24] C. Zhang, M. Rezavand, X. Hu, Dual-criteria time stepping for weakly compressible smoothed particle hydrodynamics, *Journal of Computational Physics* 404 (2020) 109135.
- [25] L. Zhan, C. Peng, B. Zhang, W. Wu, A SPH framework for dynamic interaction between soil and rigid body system with hybrid contact method, *International Journal for Numerical and Analytical Methods in Geomechanics* 44 (10) (2020) 1446–1471.
- [26] A. Combescure, B. Maurel, S. Potapov, Modelling dynamic fracture of thin shells filled with fluid: a fully SPH model, *Mechanics & Industry* 9 (2) (2008) 167–174.
- [27] S. Seo, O. Min, J. Lee, Application of an improved contact algorithm for penetration analysis in SPH, *International Journal of Impact Engineering* 35 (6) (2008) 578–588.
- [28] M. R. I. Islam, C. Peng, A total Lagrangian SPH method for modelling damage and failure in solids, *International Journal of Mechanical Sciences* 157 (2019) 498–511.
- [29] R. Gutfraind, S. B. Savage, Smoothed particle hydrodynamics for the simulation of broken-ice fields: Mohr–Coulomb-type rheology and frictional boundary conditions, *Journal of Computational Physics* 134 (2) (1997) 203–215.

- [30] H. H. Bui, J. K. Kodikara, A. Bouazza, A. Haque, P. G. Ranjith, A novel computational approach for large deformation and post-failure analyses of segmental retaining wall systems, *International Journal for Numerical and Analytical Methods in Geomechanics* 38 (13) (2014) 1321–1340.
- [31] X. Dong, G. Liu, Z. Li, W. Zeng, A smoothed particle hydrodynamics (SPH) model for simulating surface erosion by impacts of foreign particles, *Tribology International* 95 (2016) 267–278.
- [32] B. Maurel, S. Potapov, J. Fabis, A. Combescure, Full sph fluid–shell interaction for leakage simulation in explicit dynamics, *International journal for numerical methods in engineering* 80 (2) (2009) 210–234.
- [33] Y.-X. Peng, A.-M. Zhang, S.-P. Wang, Coupling of WCSPH and RKPM for the simulation of incompressible fluid–structure interactions, *Journal of Fluids and Structures* 102 (2021) 103254.
- [34] S.-B. Li, A.-M. Zhang, J.-P. Xiao, Y.-X. Peng, M.-K. Li, An algorithm for implementing a boundary viscous force with single-layer wall particles based on WCSPH, *Journal of Computational Physics* 464 (2022) 111328.
- [35] T. Gao, L. Fu, A three-dimensional meshless fluid–shell interaction framework based on smoothed particle hydrodynamics coupled with semi-meshless thin shell, *Computer Methods in Applied Mechanics and Engineering* 429 (2024) 117179.
- [36] T. Bao, J. Hu, S. Wang, C. Huang, Y. Yu, A. Shakibaeinia, An entirely SPH-based FSI solver and numerical investigations on hydrodynamic

- characteristics of the flexible structure with an ultra-thin characteristic, *Computer Methods in Applied Mechanics and Engineering* 431 (2024) 117255.
- [37] A. Leroy, D. Violeau, M. Ferrand, C. Kassiotis, Unified semi-analytical wall boundary conditions applied to 2-D incompressible SPH, *Journal of Computational Physics* 261 (2014) 106–129.
- [38] C. Zhang, M. Rezavand, Y. Zhu, Y. Yu, D. Wu, W. Zhang, S. Zhang, J. Wang, X. Hu, SPHinXsys: An open-source meshless, multi-resolution and multi-physics library, *Software Impacts* 6 (2020) 100033.
- [39] J. P. Morris, P. J. Fox, Y. Zhu, Modeling low Reynolds number incompressible flows using SPH, *Journal of Computational Physics* 136 (1) (1997) 214–226.
- [40] Y. S. Uflyand, Wave Propagation by Transverse Vibrations of Beams and Plates, *PMM: Journal of Applied Mathematics and Mechanics* 12 (1948) 287–300.
- [41] R. Mindlin, Influence of rotatory inertia and shear on flexural motions of isotropic, elastic plates, *Journal of Applied Mechanics* 18 (1951) 31–38.
- [42] D. Wu, C. Zhang, X. Hu, An SPH formulation for general plate and shell structures with finite deformation and large rotation, *Journal of Computational Physics* 510 (2024) 113113.
- [43] C. Zhang, X. Hu, N. A. Adams, A weakly compressible SPH method based on a low-dissipation riemann solver, *Journal of Computational Physics* 335 (2017) 605–620.

- [44] R. Vignjevic, J. R. Reveles, J. Campbell, SPH in a total Lagrangian formalism, *CMC-Tech Science Press*- 4 (3) (2006) 181.
- [45] L. Verlet, Computer" experiments" on classical fluids. i. thermodynamical properties of lennard-jones molecules, *Physical review* 159 (1) (1967) 98.
- [46] J. J. Monaghan, Smoothed particle hydrodynamics, In: *Annual review of astronomy and astrophysics* 30 (1992) 543–574.
- [47] H. Wendland, Piecewise polynomial, positive definite and compactly supported radial functions of minimal degree, *Adv. Comput. Math.* 4 (1) (1995) 389–396.
- [48] G. Fourey, C. Hermange, D. Le Touzé, G. Oger, An efficient fsi coupling strategy between smoothed particle hydrodynamics and finite element methods, *Computer Physics Communications* 217 (2017) 66–81.
- [49] Q. Yang, V. Jones, L. McCue, Free-surface flow interactions with deformable structures using an sph–fem model, *Ocean engineering* 55 (2012) 136–147.
- [50] K. Liao, C. Hu, M. Sueyoshi, Free surface flow impacting on an elastic structure: Experiment versus numerical simulation, *Applied Ocean Research* 50 (2015) 192–208.
- [51] C. Zhang, Y. Zhu, X. Hu, An efficient multi-resolution SPH framework for multi-phase fluid-structure interactions, *Science China Physics, Mechanics & Astronomy* 66 (10) (2023) 104712.

- [52] F. M. White, J. Majdalani, *Viscous fluid flow*, Vol. 3, McGraw-Hill New York, 2006.
- [53] C. Brehm, C. Hader, H. F. Fasel, A locally stabilized immersed boundary method for the compressible navier–stokes equations, *Journal of Computational Physics* 295 (2015) 475–504.
- [54] M. Al-Marouf, R. Samtaney, A versatile embedded boundary adaptive mesh method for compressible flow in complex geometry, *Journal of Computational Physics* 337 (2017) 339–378.
- [55] C. Liu, X. Zheng, C. Sung, Preconditioned multigrid methods for unsteady incompressible flows, *Journal of Computational physics* 139 (1) (1998) 35–57.
- [56] D.-V. Le, B. C. Khoo, J. Peraire, An immersed interface method for viscous incompressible flows involving rigid and flexible boundaries, *Journal of Computational Physics* 220 (1) (2006) 109–138.
- [57] D. Russell, Z. J. Wang, A cartesian grid method for modeling multiple moving objects in 2d incompressible viscous flow, *Journal of Computational Physics* 191 (1) (2003) 177–205.
- [58] S. Zhang, W. Zhang, C. Zhang, X. Hu, A lagrangian free-stream boundary condition for weakly compressible smoothed particle hydrodynamics, *Journal of Computational Physics* 490 (2023) 112303.
- [59] Y. Zhu, C. Zhang, X. Hu, A dynamic relaxation method with operator splitting and random-choice strategy for SPH, *Journal of Computational Physics* 458 (2022) 111105.

- [60] B. Yang, T. A. Laursen, A large deformation mortar formulation of self contact with finite sliding, *Computer Methods in Applied Mechanics and Engineering* 197 (6-8) (2008) 756–772.
- [61] M. Tian, R. Li, X. Zhang, M. Jin, Collision simulation of GQ70 light oil tank car at the level crossing, in: *Advances in Mechanical Design: Proceedings of the 2019 International Conference on Mechanical Design (2019 ICMD)*, Springer, 2020, pp. 623–633.